J Seismol (2026) 30:103
https://doi.org/10.1007/s10950-026-10446-9

RESEARCH

Kinematic evolution of the Northern Red Sea Region inferred from probabilistic moment tensor summation

Ali Abdelfattah · Mohamed Ezzelarab · Chokri Jallouli · Hassan Alzahrani

Received: 2 March 2026 / Accepted: 23 August 2026
© The Author(s), under exclusive licence to Springer Nature B.V. 2026

Abstract We present a probabilistic assessment of present-day crustal deformation by integrating seismic moment-tensor summation with nonparametric bootstrap resampling of focal mechanisms and seismicity parameters across three distinct zones: The Gulf of Suez, the northern Red Sea axial rift, and the Gulf of Aqaba. By explicitly propagating uncertainties associated with focal-mechanism geometry (strike, dip, rake) and seismicity parameters (a, b-values, and Mmax), we derive statistically robust moment, strain-rate, and model-equivalent velocity tensors for each domain. The results reveal weak but measurable seismic deformation in the Gulf of Suez (strain-rate magnitude ~ 10^{-7} yr^{-1}), still lower and more heterogeneous extension in the northern Red Sea (~ 10^{-9} yr^{-1}), and the strongest strike-slip to transtensional deformation in the Gulf of Aqaba (~ 10^{-6} yr^{-1}). These tensors are independently corroborated by published focal-mechanism stress inversions, with which they share consistent deformation styles and principal-axis orientations. Although seismicity may occur due to stress transfer or reactivation triggered by earthquakes from adjacent active source zones, the results indicate a regional transition from an earlier Red Sea–Suez rifting phase toward markedly decelerated rifting in both the Gulf of Suez and the northern Red Sea, while active deformation localizes along the Gulf of Aqaba. The systematic discrepancy between seismic and geodetic deformation indicates that a substantial fraction of the total plate-boundary strain is accommodated aseismically through fault creep, dyking, and viscous lower-crustal flow, with direct implications for seismic hazard assessment across the region. Bootstrap convergence diagnostics confirm stable resolution of the dominant deformation style in each tectonic domain while preserving physically meaningful uncertainty where deformation is intrinsically weak or heterogeneous. Collectively, these results demonstrate that the Sinai triple junction operates as a diffuse plate boundary in which deformation is strongly partitioned between transform shear, waning rifting, and weakly coupled axial extension, with aseismic processes playing a key role in accommodating plate motions. The velocity tensors are treated as model-equivalent kinematic quantities derived from the seismic moment budget and are therefore interpreted together with the moment and strain-rate tensors, rather than as direct GPS-equivalent opening or slip rates.

Keywords Seismic strain rate · Aseismic deformation · Focal-mechanism bootstrap · Gutenberg–Richter uncertainty · Probabilistic tectonics · Sinai triple junction

Supplementary Information The online version contains supplementary material available at https://doi.org/10.1007/s10950-026-10446-9.

A. Abdelfattah (✉) · C. Jallouli · H. Alzahrani
Department of Geology and Geophysics, King Saud University, Riyadh 11451, Kingdom of Saudi Arabia
e-mail: aabdelfattah@ksu.edu.sa; ali_kamel100@yahoo.co.uk

M. Ezzelarab
Seismology Department, National Research Institute of Astronomy and Geophysics, Helwan, Cairo, Egypt

Published online: 30 September 2026

1 Introduction

The Red Sea is one of the few places on Earth where a new plate boundary is actively forming, providing a rare natural laboratory for examining the transition from continental rifting to incipient ocean spreading (Almalki et al. 2015; Augustin et al. 2021; Artemieva et al. 2022). The system displays two enigmatic asymmetries that no single geodynamic framework has yet been able to fully reconcile. Along strike, mature seafloor spreading dominates the southern Red Sea, where oceanic crust began forming at ~ 12–13 Ma (Izzeldin 1987; Augustin et al. 2021), whereas the segment north of ~ 20–22°N persists in continental rifting, as evidenced by the absence of rift-parallel marine magnetic anomalies (Coleman and McGuire 1988; Cochran 2005; Schettino et al. 2016). Across strike, rift-related Cenozoic volcanism in the north is conspicuously displaced 200–400 km eastward into the Arabian shield rather than localized beneath the rift axis (Camp and Roobol 1992; Chang et al. 2011; Bosworth et al. 2016). Competing geodynamic models, invoking either northward channeling of Afar plume material (Ebinger and Sleep 1998; Park et al. 2007; Chang et al. 2011; Koptev et al. 2018; Petrunin et al. 2020) or far-field stresses associated with Arabia–Africa separation, Mediterranean subduction, or Zagros slab pull (Voggenreiter et al. 1988; McGuire and Bohannon 1989; McQuarrie et al. 2003; Reilinger and McClusky 2011; Yao et al. 2017), each capture only part of the picture. Notably, regional seismic studies reveal no upper-mantle hotspot anomaly beneath the north-central Red Sea (Park et al. 2007; Chang et al. 2011; Yao et al. 2017; Kaviani et al. 2020), and the perpendicular orientation of vertical gravity gradient (VVG) belts to the rift axis in this segment is inconsistent with seafloor spreading, contrasting sharply with axis-parallel VVG belts in the actively spreading south (Augustin et al. 2021).

The northernmost Red Sea and its adjoining margins form a tectonically complex triple junction in which extension, shear, and transtension interact within a diffuse plate boundary. Resolving deformation in such settings requires reconciling observations that sample different timescales and mechanical regimes. Space-geodetic data integrate both brittle and ductile deformation with high precision, whereas earthquake catalogs capture only the brittle seismic component and are inherently incomplete. The bifurcation of the system into the Gulf of Suez and the Gulf of Aqaba adjoins three contrasting zones within a single tectonic structure: a transform boundary (the Gulf of Aqaba–Dead Sea Transform), a waning rift (the Gulf of Suez), and an active axial rift characterized by magmatism and thinned lithosphere (the northern Red Sea). In the axial rift, brittle extension inferred from seismicity and faulting may be partially compensated by magmatic underplating, which adds crustal material at depth and complicates straightforward interpretations of crustal thinning (Thybo and Nielsen 2009). This setting raises two central seismological questions: how is strain partitioned between seismic and aseismic processes across these contrasting zones, and to what extent can seismicity alone resolve the prevailing deformation regime. Regions of prolonged extension are often associated with crustal thinning, as reflected in Moho topography. However, extension does not inevitably imply thinning; magmatic underplating, particularly in rift settings, can compensate for stretching by adding new igneous material at the base of the crust, thereby preserving or increasing crustal thickness (Thybo & Nielsen 2009; Corti 2009).

Previous studies have addressed individual components of the system using either geodetic velocities (McClusky et al. 2003; Reilinger et al. 2006; ArRajehi et al. 2010; Castro-Perdomo et al. 2022) or earthquake focal mechanisms (Badawy and Horvath 1999; Salamon et al. 2003; Abdelazim et al. 2023). However, a unified probabilistic seismic strain-rate assessment spanning all three arms of the triple junction is still lacking. As a consequence, the spatial variability of deformation style, the degree to which the Gulf of Suez is tectonically waning or aseismic, the heterogeneity of extension across the northern Red Sea, and the localization of compression within the transtensional Gulf of Aqaba remain only partially constrained. Robust quantification of seismic strain rates, together with their associated uncertainties, is essential not only for refining geodynamic models of the northern Red Sea region but also for assessing seismic hazard across the densely populated and tectonically active margins of the region.

In this study, we apply probabilistic moment tensor summation (PMTS) with bootstrap resampling of focal mechanisms to quantify regional strain-rate tensors and model-equivalent velocity tensors across the Sinai

triple junction. By explicitly propagating uncertainties in focal-mechanism geometry (strike, dip, rake) and seismicity statistics (a- and b-values, and Mmax), we derive statistically robust constraints on deformation style, deformation-axis orientations, and rate. The P- and T-axes are used as deformation axes and stress-orientation proxies, but the study does not claim to replace a full formal stress-tensor inversion. The approach enables us to (1) distinguish extensional, shear-dominated, and compressional components within each sub-domain; (2) assess whether deformation is dominated by crustal thinning, thickening, or lateral shear; and (3) estimate the seismic deficit through comparison with GPS-derived deformation fields. By linking the seismic component of deformation to underlying geodynamic processes, including magmatic intrusion, viscous lower-crustal flow, and aseismic fault creep, the obtained results provide a probabilistic basis for seismic hazard assessment across the Gulf of Aqaba. This clarification is important because the velocity tensor expresses the displacement implied by the seismic moment-release model under the adopted source-volume assumptions, not the full interseismic velocity field measured by GPS.

2 Geological and geodynamic settings

The Arabia–Nubia plate boundary-initiated Neogene rifting along the Red Sea as a consequence of the broader Afro-Arabian tectonic reorganization that occurred following the breakup of Gondwana (Bosworth 2015; McClusky et al. 2003; Reilinger et al. 2006). Northward, this rift system evolves into a diffuse plate boundary where extensional, strike-slip, and transtensional regimes overlap (Reilinger et al. 2006; ArRajehi et al. 2010). The northern Red Sea, Gulf of Suez, and Gulf of Aqaba thus constitute a triple-junction zone where deformation partitioning reflects both inherited crustal architecture and ongoing plate kinematics (Bosworth and McClay 2001; Reilinger et al. 2006; Le Béon et al. 2008; ArRajehi et al. 2010). Recent geodynamic modeling further suggests that the north-central Red Sea rift may be a transient extensional feature whose future spreading axis could shift eastward into Arabia rather than simply propagate northward along the present rift axis (Artemieva et al. 2022). Figure 1 shows major tectonic regime in the region.

In the Gulf of Suez, rift morphology and fault-block topography remain well preserved, yet the region shows waning tectonic activity. Basin-analysis and geomorphic studies indicate that major rift opening and tectonic subsidence decreased sharply after the Middle Miocene, although very slow Quaternary extension may persist (Richardson & Arthur 1988; Bosworth et al. 2005; Fernández-Blanco et al. 2025; Moawad et al. 2025). Fault-plane solutions reveal predominantly normal faulting with NW–SE oriented tension axes, while subdued seismic moment release suggests that much of the regional strain is now accommodated aseismically or has migrated toward adjacent domains. Importantly, the present results show even lower earthquake-derived deformation in the northern Red Sea than in the Gulf of Suez. The northern Red Sea should therefore not be treated simply as a more active continuation of the rift; rather, it may represent a weakly coupled, transient, or decelerating rift segment in which extension is partitioned among small earthquakes, magmatic processes, and possible eastward migration of the future plate boundary (El Khrepy et al. 2021; Artemieva et al. 2022).

These distinct tectonic domains collectively form a diffuse triple-junction in which extension, shear, and transtension interact within a complex stress field. Lateral variations in lithospheric thickness, crustal composition, and thermal regime lead to sharp contrasts in rheological behavior from brittle fault-controlled shear zones in the Aqaba–DST fault to ductile flow and magmatic accommodation in the northern Red Sea rift axis. Variations in gravitational potential energy driven by crustal thinning and topographic gradients further modulate the regional deviatoric stress distribution (Ben-Avraham et al. 2008; Bosworth et al. 2005; Morley 1999). Consequently, the spatial heterogeneity of stress and strain observed across the northern Red Sea–Gulf of Suez–Gulf of Aqaba region arises from the combined effects of (1) decelerated or weakly seismic rifting within the northern Red Sea and Gulf of Suez, (2) localized shear and transtension along cooler, brittle transform faults in the Gulf of Aqaba, and (3) transitional zones where deformation is partitioned between seismic fault slip and aseismic lower-crustal or magmatic processes. These conditions provide the geodynamic setting underpinning the probabilistic moment-tensor summation and strain-rate analysis developed below.

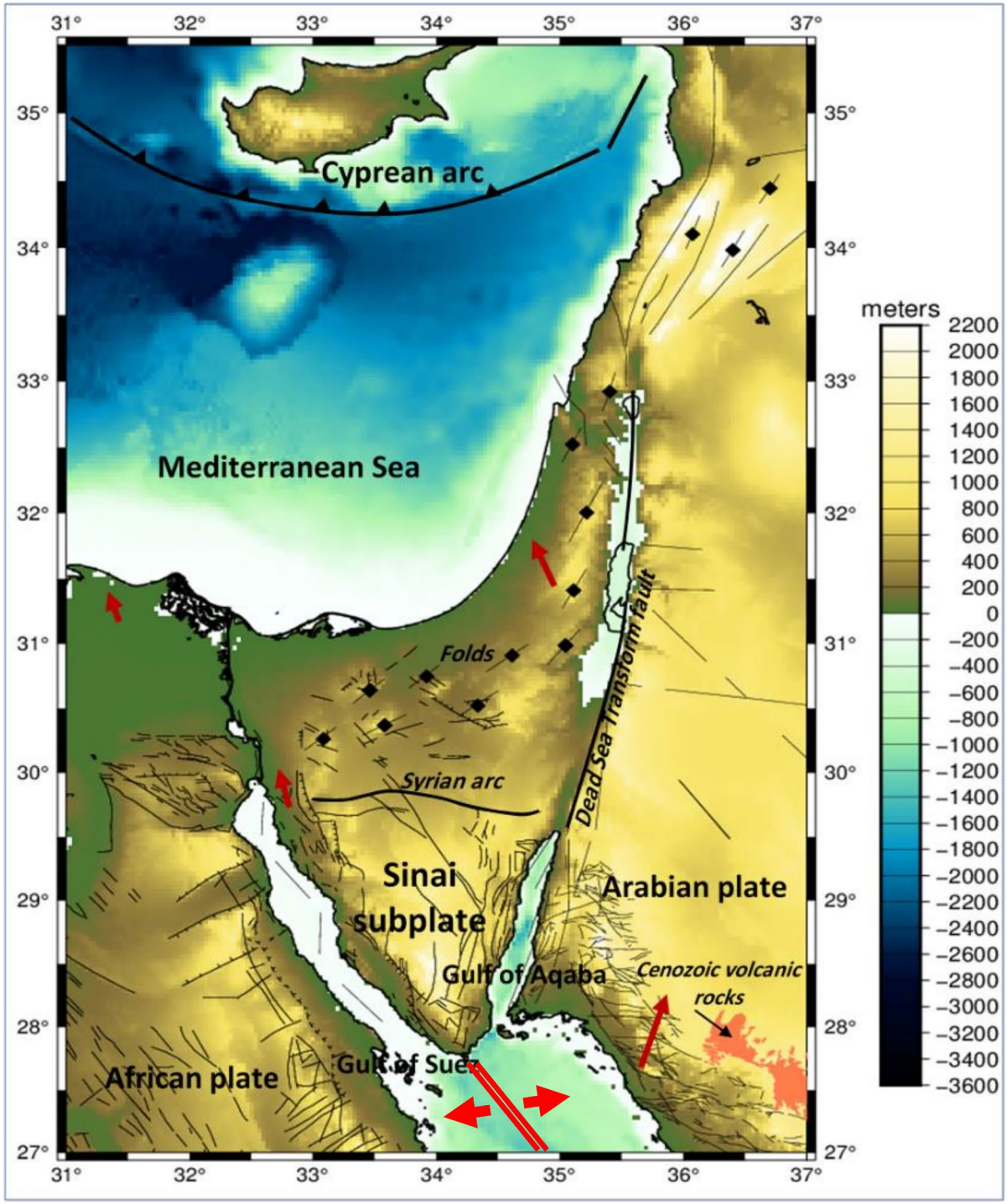


Fig. 1 Topographic map of the Sinai Peninsula and surrounding region showing major tectonic elements: fold axes, shear zones, and faults (after Hamimi et al. 2020; Said 2017). Thick red arrows indicate plate motions relative to Eurasia (Reilinger et al. 2006; ArRajehi et al. 2010); arrow lengths are proportional to velocity magnitude

The three seismogenic source zones shown in Fig. 2 (Gulf of Suez, northern Red Sea Rift, Gulf of Aqaba) were delineated based on tectonic environment, spatial clustering of seismicity, and fault patterns from focal mechanisms. Earthquakes falling outside these polygons (approximately 15% of the 13,005 events in the compiled catalog) were excluded from the zone-specific moment tensor summation. These excluded events are located in: (1) the Sinai intraplate interior, where seismicity is sparse and diffuse, (2) the eastern Mediterranean shelf, where deformation is dominated by the Cyprus Arc rather than the Red Sea system, and (3) the Gulf of Suez mouth region, where transitional tectonics between the rift and the Mediterranean complicates single-regime assignment. Including these events would introduce contamination from deformation styles unrelated to the Red Sea-Dead Sea transform system, which is the focus of this study. The 15% exclusion fraction is comparable to or smaller than similar regional seismic deformation studies (e.g., the Arabia-Eurasia collision zone; Reilinger et al. 2006; Masson et al. 2015).

3 Data and methodology

Probabilistic moment-tensor summation (PMTS) was performed for three sub-domains of the Sinai triple junction, the Gulf of Suez, the northern Red Sea axial rift, and the Gulf of Aqaba, using a compiled focal-mechanism catalog that integrates published solutions and Egyptian National Seismological Network (ENSN) bulletin entries. For each of the three zones shown in Fig. 2, we selected earthquake catalog events ($M \geq 3.0$) and focal mechanisms with hypocenters located within the polygon boundaries that define the structural extent of each zone. This selection minimizes the influence of sparse and diffuse seismicity, which often carries larger uncertainties in hypocenter determination. Events outside these polygons were excluded from the zone-specific moment tensor summations but are displayed in Fig. 2 to provide a complete view of the regional seismicity.

The seismic source zones were delineated from tectonic setting, spatial clustering of historical earthquakes, earthquake epicenter distributions, and focal-mechanism patterns. For each zone, geometric parameters (length, width, and seismogenic thickness) were estimated from hypocentral distributions in relocated earthquake catalogs. Seismic recurrence parameters, including Gutenberg-Richter a- and b-values and maximum magnitude (Mmax), were compiled from published probabilistic seismic hazard and regional seismicity studies. For the Gulf of Aqaba, the b-value and adopted Mmax of 7.3 are constrained by the historical record of large earthquakes along the Dead Sea Transform system (Al-Shijbi et al. 2019; El-Hussain et al. 2018). The Gulf of Suez, a mature and strongly decelerated rift, is represented by a relatively high b-value and a lower Mmax of 6.5 (Abdalzaher et al. 2020). For the northern Red Sea Rift Zone, Mmax is adopted as 7.0 following Al-Ahmadi et al. (2014), but the tensor results are interpreted as a low-seismic-strain signal that may reflect waning rifting, aseismic/magmatic accommodation, or future relocation of the extensional axis. The seismogenic source zone parameters and recurrence characteristics are listed in Table 1. Because the moment-rate estimate is sensitive to the adopted Gutenberg-Richter parameters, especially Mmax and b-value, the numerical strain-rate amplitudes are interpreted together with their bootstrap uncertainty ranges and with the relative ranking among the three tectonic domains. The mainconclusions rely on the stable principal-axis geometries and on the order-of-magnitude contrast between domains, rather than on a single deterministic choice of recurrence parameters.

The style and orientation of tectonic deformation are directly provided by a compiled catalog of earthquake focal mechanisms. This study integrates mechanisms from key publications spanning over two decades, ensuring a robust sample of crustal stress release. The catalog includes solutions from early regional compilations (Badawy and Horváth 1999; Hofstetter et al. 2007), mechanisms from significant specific events (Salamon et al. 2003), and many modern, precisely calculated moment tensor solutions from Hussein et al. (2013), Abu El-Nader and Hussein (2018), Badreldin et al. (2019), Ali and Badreldin (2019) and Abd El-Aal et al. (2019). This collective dataset provides the strike (φ), dip (δ), and rake (λ) angles for the double-couple component of each seismic event, which are the direct inputs for calculating seismic moment tensors. The mechanisms clearly illustrate the dominant left−lateral strike−slip motion in the Gulf of Aqaba, the normal faulting in the Gulf of Suez and the northern Red Sea Rift, and the transitions between these styles. The seismicity and dataset of the focal mechanism solutions are presented in Fig. 2, while

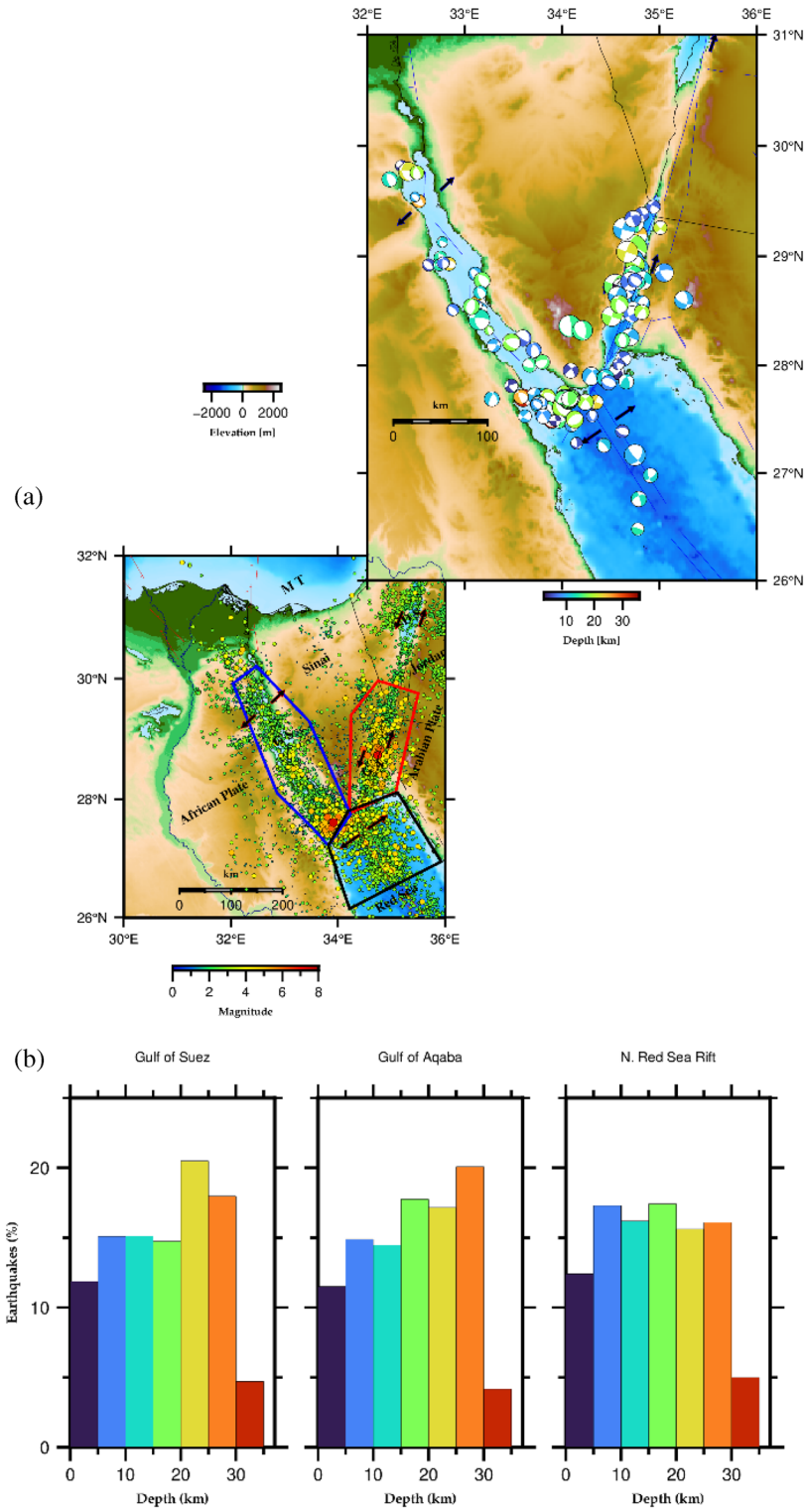


Fig. 2 **a** Map of the northern Red Sea region showing the three seismogenic zones analyzed in this study: Gulf of Suez (blue polygon), northern Red Sea Rift (black polygon), and Gulf of Aqaba (red polygon). Earthquake epicenters (1900–2023) are shown as colored circles, scaled by magnitude. Focal mechanism solutions are displayed as beachballs, color-coded by depth. Arrows indicate relative plate motions derived from GPS observations (Reilinger et al. 2006). **b** Depth histograms of seismicity within each polygon

Table 1 Seismogenic Source Zone Parameters and Recurrence Characteristics

Source Zone	Seismogenic Zone Parameters			Seismicity Parameters			References
	Length (km)	Width (km)	Thickness (km)	a-value	b-value	M max	
Gulf of Aqaba	180	25	20–25	4.2	0.85	7.3	Sawires et al. (2016a); Sawires and Peláez (2025); Deif et al. (2017)
Gulf of Suez	300	40	15–20	3.8	1	6.5	Sawires et al. (2016b); Ezzelarab et al. (2016)
N. Red Sea Rift	200	30	20–25	4	0.9	7	Al-Ahmadi et al. (2014); Ibrahim et. al (2021)

the dataset, including the event date, location, magnitude, and focal mechanism parameters (strike, dip, and rake), is provided in Table 2. Figure 2 shows the earthquake epicenters from the 1900–2023 catalogue and the corresponding focal mechanism solutions as a function of depth, along with depth histograms for each seismic zone. Polygons are drawn to enclose the three primary tectonic domains of the Sinai triple junction: the Gulf of Suez, the northern Red Sea axial rift, and the Gulf of Aqaba. Earthquakes located outside these polygons (e.g., intraplate events in the Sinai Peninsula or Eastern Desert, off-axis seismicity) are excluded from the moment-tensor summation because they do not represent the focused deformation associated with the triple junction arms. Their exclusion does not alter the main results, as they contribute negligible strain compared to the within-polygon events.

3.1 Theoretical background

The present analysis employs a probabilistic seismic moment-tensor approach combined with bootstrap uncertainty propagation to quantify crustal deformation and its associated uncertainties across the northern Red Sea and adjacent regions. The methodology follows and extends the method of Kiratzi et al. (2018), integrating both deterministic and stochastic components to ensure statistically robust deformation estimates. The approach involves transforming focal mechanisms into moment tensors, estimating the moment-rate tensor and associated strain-rate field, and propagating uncertainties through Monte Carlo and bootstrap procedures. The key concept is to use bootstrap resampling of input parameters, specifically, focal mechanisms and earthquake locations, to capture the inherent variability in the dataset. Each bootstrap realization is used to recompute the deformation tensors (moment, strain-rate, and velocity), producing an ensemble of results from which credible intervals and posterior statistics are derived. This probabilistic technique ensures that both epistemic (model) and aleatory (data) uncertainties are explicitly incorporated into the final deformation parameters.

For each earthquake, the seismic moment tensor is derived from the focal mechanism parameters (strike ϕ, dip δ, rake λ, and scalar moment M_0) using the double-couple formulation (Aki and Richards (1980) and Kiratzi et al., (2018)):

$$\begin{aligned} M_{xx} &= -M_0\left(\sin\delta\cos\lambda\sin 2\phi + \sin 2\delta\sin\lambda\sin^2\phi\right)\\ M_{yy} &= M_0\left(\sin\delta\cos\lambda\sin 2\phi - \sin 2\delta\sin\lambda\cos^2\phi\right)\\ M_{zz} &= M_0(\sin 2\delta\sin\lambda)\\ M_{xy} &= M_0(\sin\delta\cos\lambda\cos 2\phi + 0.5\sin 2\delta\sin\lambda\sin 2\phi)\\ M_{xz} &= -M_0(\cos\delta\cos\lambda\cos\phi + \cos 2\delta\sin\lambda\sin\phi)\\ M_{yz} &= -M_0(\cos\delta\cos\lambda\sin\phi - \cos 2\delta\sin\lambda\cos\phi) \end{aligned} \tag{1}$$

Each tensor is normalized by its scalar moment, yielding ($\overline{M}_{ij}$), the normalized moment tensor for event k. The zone-averaged normalized tensor is then computed as:

$$\overline{M}_{ij} = \frac{1}{N}\sum_{k=1}^{N}\widehat{M}_{ij}^{k} \tag{2}$$

where N is the number of earthquakes within the zone, and ($\widehat{M}_{ij}^{k}$) represents the normalized moment tensor of the k^{th} event. Because the available catalog does not span multiple recurrence intervals of the largest earthquakes, the moment rate ($\dot{M}_o$) is estimated following Molnar (1979) from the earthquake size distribution:

$$\dot{M}_o = \frac{A}{1-B}M_{o,max}^{(1-B)} \tag{3}$$

where A and B are auxiliary constants derived from the Gutenberg-Richter recurrence parameters and

Table 2 Focal-mechanism parameters for seismogenic source zones

Gulf of Aqaba										
ID	**Date**	**To**	**Lat [o]**	**Long [o]**	**d [km]**	**Mw**	**strike**	**dip**	**rake**	**Mo**
1	19820323	104800	27.9	34.3	10	4.7	220	65	−40	2.86E+22
2	19830203	134604.9	29.19	34.77	24	5.3	360	80	14	2.31E+23
3	19851231	194241	28.85	35.05	9	4.8	155	60	−30	4.06E+22
4	19890909	0	28.57	34.82	10	4.1	205	50	−110	3.56E+21
5	19,930703	233410	28.86	34.82	18	4.7	114.17	88.69	149.41	2.86E+22
6	19930803	124305	28.73	34.55	17	6	7	62	−117	2.63E+24
7	19930803	124314	28.73	34.55	17	6.1	293.54	87.27	−157.17	3.72E+24
8	19930803	163323	28.36	34.08	15	5.7	356.13	79.41	−82.81	9.27E+23
9	19930807	45540	28.61	34.63	10	4.2	216.57	50.19	−42.41	5.04E+21
10	19930820	230959	28.72	34.61	2	4.6	116.24	79.84	140.06	2.02E+22
11	19931103	183932	28.7	34.65	7	4.9	86.2	76.13	−148.33	5.74E+22
12	19931108	10602	28.69	34.65	8	4.7	303.34	80.49	−119.89	2.86E+22
13	19931204	233411	28.89	34.8	10	4.6	93.21	68.07	−147.59	2.02E+22
14	19951122	1526	29.07	34.73	18	7.2	196	59	−15	1.71E+26
15	19951122	124704	29.3	34.74	15	5	73.99	80.04	−150.11	8.13E+22
16	19951122	221657	28.32	34.21	15	5.2	357.43	60.54	−68.49	1.63E+23
17	19951123	717	29.25	34.64	10	5.7	199	77	7	9.27E+23
18	19951124	164345	28.97	34.74	10	4.9	164.49	54.28	−68.04	5.74E+22
19	19951211	13208	28.92	34.75	19	5	302	84	146.79	8.13E+22
20	19960103	100526	28.6	35.25	10	4.8	113.43	59.77	−137.83	4.06E+22
21	19960108	1318	29.38	34.82	6	3.8	339.96	78.86	164.2	1.25E+21
22	19960116	61700	29.34	34.73	6	4.3	158.64	82.79	148.51	7.13E+21
23	19960204	72300	29.45	34.94	6	3.6	293.84	77.43	−148.5	6.25E+20
24	19960221	5951	28.8	34.78	10	5.3	132	30	−104	2.31E+23
25	19970510	147	28.26	34.7	10	4.6	114	89	150	2.02E+22
26	20000308	142226	28.83	34.73	15	4.9	182	48	−48	5.74E+22
27	20000308	122229	28.64	34.57	10	4.8	198	31	−18	4.06E+22
28	20000308	142225	28.77	34.7	7	4.9	134.95	85.1	−169.32	5.74E+22
29	20000406	63734	28.78	34.83	12	4.8	19.99	85.1	−12.08	4.06E+22
30	20000803	142225	28.64	34.57	10	4.8	107.59	82.31	166.45	4.06E+22
31	20010207	33900	29.26	35.01	21	3.6	44	80	−5	6.25E+20
32	20021110	5945	28.23	34.62	16	3.9	180.27	47.3	−83.94	1.77E+21
33	20040922	120023	28.45	34.6	10.3	3.2	270.22	64.05	−76.21	1.56E+20
34	20050120	134100	28.5	34.66	18.8	3.2	41	43	−56	1.56E+20
35	20080302	170600	28.76	34.79	13.7	3.2	58	75	−29	1.56E+20
36	20080404	140500	28.78	34.75	6.9	3.7	145	46	−67	8.85E+20
37	20111021	123700	28.52	34.73	9	3.7	148	49	−147	8.85E+20
38	20130610	84400	28.06	34.63	6.1	3.9	142	73	−15	1.77E+21
39	20150627	53404	29.04	34.67	22	5.6	200	82	2	6.55E+23
40	20160516	14200	28.47	34.72	7.35	4.3	157	52	−173	7.13E+21
41	20160516	4559	28.45	34.51	18	5.2	19	88	−3	1.63E+23
42	20160813	30600	28.49	34.82	19.1	3.9	332	47	−153	1.77E+21
43	20161129	113	28.56	34.59	18	4.7	188	59	−44	2.86E+22
44	20170519	141600	27.94	34.56	3.55	4.1	304	50	−27	3.56E+21

Table 2 (continued)

Gulf of Aqaba										
ID	**Date**	**To**	**Lat [o]**	**Long [o]**	**d [km]**	**Mw**	**strike**	**dip**	**rake**	**Mo**
Gulf of Suez										
ID	**Date**	**To**	**Lat [o]**	**Long [o]**	**d [km]**	**Mw**	**strike**	**dip**	**rake**	**Mo**
1	30656	0.5	28.55	33.13	24	4.8	129	86	−10	4.06E+22
2	30657	0.4375	28.51	33.16	10	3.8	157	78	−51	1.25E+21
3	30658	0.377778	28.84	33.11	10	3.5	320	53	−99	4.42E+20
4	30659	0.459722	28.78	33.18	17	4.2	155	57	−66	5.04E+21
5	30660	0.509028	29.7	32.23	13	4	166	62	−69	2.51E+21
6	30661	0.333333	28.25	33.6	6	4.3	122	77	−109	7.13E+21
7	30662	0.779861	28.55	33.12	7	3.1	311	80	−23	1.1E+20
8	30663	0.804167	28.21	33.48	18	4.6	257	52	−129	2.02E+22
9	30664	0.888194	28.93	32.84	23	3.5	120	46	−75	4.42E+20
10	30665	0.791667	28.67	33.16	12	3.4	167	57	−66	3.12E+20
11	30666	0.479861	28.92	32.63	5	3.2	318	55	−84	1.56E+20
12	30667	0.648611	28.51	32.88	7.5	3.2	310	65	−101	1.56E+20
13	30668	0.333333	29.13	32.77	12	2.8	288	75	−133	3.87E+19
14	30669	0.834722	28.99	32.75	14	3.3	174	66	−51	2.2E+20
15	30670	0.604167	28.92	32.74	14	3.1	118	58	−48	1.1E+20
16	30671	0.634722	29.82	32.35	4	3.1	90	68	−133	1.1E+20
17	30672	0.509028	29.5	32.53	25	3.5	323	52	−71	4.42E+20
18	30673	0.376389	28.94	32.78	7	3.2	182	76	−48	1.56E+20
19	30674	0.272222	28.47	33.1	13.6	3.4	308	53	−63	3.12E+20
20	30675	0.138194	28.32	33.25	17.6	2.4	304	30	−133	9.64E+18
21	30676	0.161111	29.54	32.49	10	2.6	143	46	−69	1.93E+19
22	30677	0.831944	28.14	33.71	8.1	3.93	189	59	−61	1.97E+21
23	30678	0.838194	28.18	33.3	9.8	3.5	284	67	−32	4.42E+20
24	30679	0.024306	28.43	33.15	23	3.99	193	69	−30	2.43E+21
25	30680	0.163889	27.81	33.48	4.2	3.51	154	62	−17	4.57E+20
26	30681	0.492361	28.42	33.15	13.3	5.45	171	55	−21	3.89E+23
27	30682	0.127083	29.77	32.42	22	4.9	275	79	−124	5.74E+22
28	30683	0.040972	29.76	32.51	19.03	3.65	333	55	−116	7.44E+20
29	30684	0.38125	28.54	33.07	17.02	4.22	198	38	−83	5.4E+21
30	30685	0.302083	27.61	33.91	12	6.7	113	53	−91	3E+25
31	30686	0.009028	27.6	33.9	33	4.6	165	80	−24	2.02E+22
32	30687	0.215278	27.5	33.9	33	4.6	223	65	−90	2.02E+22
33	30688	0.138889	27.7	33.6	33	4.6	154	90	−17	2.02E+22
34	30689	0.947222	27.5	33.9	33	4.4	333	80	−86	1.01E+22
35	30690	0.34375	27.55	33.82	36	4.7	93	59	−45	2.86E+22
36	30691	0.409028	27.7	33.8	12	5	121	50	−82	8.13E+22
37	30692	0.704861	27.72	33.72	10	4.1	195	81	−1	3.56E+21
38	30693	0.727083	27.75	34.02	19	3.6	321	89	−50	6.25E+20
39	30694	0.388889	27.71	33.85	20	4.1	150	62	−51	3.56E+21
40	30695	0.225694	27.6	33.86	16	3.9	321	47	−99	1.77E+21
41	30696	0.854167	27.66	33.76	14	3.6	81	52	−84	6.25E+20
42	30697	0.797222	27.61	34	19	5	146	48	−70	8.13E+22

Table 2 (continued)

Gulf of Aqaba										
ID	**Date**	**To**	**Lat [o]**	**Long [o]**	**d [km]**	**Mw**	**strike**	**dip**	**rake**	**Mo**
43	30698	0.30625	27.63	33.77	15	3.8	243	72	−154	1.25E+21
44	30699	0.479861	27.64	33.76	12	4.2	134	60	−99	5.04E+21
45	30700	0.517361	27.64	33.76	11	3.1	318	65	−172	1.1E+20
46	30701	0.604861	27.65	33.79	9	3.1	126	82	−134	1.1E+20
47	30702	0.370139	27.53	33.81	9	3.9	324	79	−141	1.77E+21
48	30703	0.88125	27.69	33.28	11	3.9	204	71	−59	1.77E+21
49	30704	0.725	27.48	33.97	16	3.4	79	76	−23	3.12E+20
50	30705	0.786111	28	33.67	15	3.7	94	63	−131	8.85E+20
51	30706	0.752778	27.53	33.62	10.2	3.4	223	79	−157	3.12E+20
52	30707	0.102778	28.03	33.8	16	3.8	261	63	−60	1.25E+21
53	30708	0.060417	27.69	34.06	18.2	4.88	169	71	−63	5.36E+22
54	30709	0.202778	27.67	34.07	17.8	4.39	145	60	−118	9.75E+21
55	30710	0.3	27.7	34.06	15	4.59	132	70	−118	1.95E+22
56	30711	0.219444	27.66	34.24	15.9	4.19	230	49	−8	4.86E+21
57	30712	0.711111	27.69	34.07	5.5	5.06	202	47	−130	1E+23
58	30713	0.342361	27.7	34.11	9.1	4.14	163	78	−59	4.09E+21
59	30714	0.395139	27.71	34.1	12	4.1	162	84	−108	3.56E+21
60	30715	0.665278	27.69	34.08	17.4	4.57	175	66	−128	1.82E+22
61	30716	0.880556	27.95	34.09	4.57	3.96	233	76	−19	2.19E+21
62	30717	0.578472	27.45	34.1	9.06	3.64	172	67	−23	7.18E+20
63	38145	0.509201	29.5	32.53	24.4	3.4	325	44	−82	3.12E+20
64	16/08/2004	0.946412	28.93	32.77	8.4	2.8	279	72	−128	3.87E+19
65	28/09/2006	0.272361	28.47	33.1	13.5	3.4	308	53	−63	3.12E+20
66	25/01/2008	0.138681	28.32	33.25	17.5	2.4	304	30	−133	9.64E+18
67	14/03/2008	0.161539	29.54	32.49	10	2.6	143	46	−69	1.93E+19
North Red Sea Rift										
ID	**Date**	**To**	**Lat [o]**	**Long [o]**	**d [km]**	**Mw**	**strike**	**dip**	**rake**	**Mo**
1	27/04/2004	0.472685	27.39	34.62	5.5	3.5	121	52	−69	4.42E+20
2	38447	0.824479	27.28	34.15	5.4	3.1	352	83	−52	1.1E+20
3	23/07/2005	0.621782	28.01	34.58	5.5	3	179	61	−22	7.76E+19
4	28/10/2005	0.708438	27.71	33.58	25	3.8	284	41	−143	1.25E+21
5	38667	0.648009	27.26	34.43	11	3.7	196	25	−32	8.85E+20
6	30/01/2006	0.148229	27.9	34.41	15	2.8	149	55	−84	3.87E+19
7	38750	0.409606	27.88	34.45	12	4.5	309	41	−124	1.43E+22
8	38872	0.457083	27.64	33.74	9.3	3	144	50	−68	7.76E+19
9	20/03/2008	0.379549	27.53	34.31	7.5	3.1	151	63	−126	1.1E+20
10	39543	0.047396	27.49	33.93	3.9	3	354	77	−10	7.76E+19
11	24/05/2008	0.026308	27.64	34.32	4	3.1	316	84	−31	1.1E+20
12	29/05/2008	0.257523	27.83	34.46	7.1	3	304	44	−73	7.76E+19
13	29/05/2008	0.303032	27.84	34.48	8.1	3.9	289	40	−92	1.77E+21
14	40594	0.060463	27.6922	34.0586	14	4.2	86	64	−146	5.04E+21
15	40594	0.203194	27.6706	34.0684	15	4.2	299	47	−105	5.04E+21
16	40724	0.451806	27.6578	34.3491	23	3.7	110	90	−10	8.85E+20
17	40866	0.300174	27.6955	34.0602	12	4.3	353	68	−125	7.13E+21

Table 2 (continued)

Gulf of Aqaba										
ID	**Date**	**To**	**Lat [o]**	**Long [o]**	**d [km]**	**Mw**	**strike**	**dip**	**rake**	**Mo**
18	40867	0.219491	27.6615	34.2423	19	4.2	220	70	−25	5.04E+21
19	40938	0.711412	27.6934	34.0645	17	4.8	135	60	−65	4.06E+22
20	40939	0.032106	27.7022	34.0647	15	3.3	11	52	−102	2.2E+20
21	40939	0.433461	27.7146	34.0082	10	3.2	195	65	−85	1.56E+20
22	41062	0.343009	27.6968	34.1135	16	3.8	120	70	−60	1.25E+21
23	41070	0.395359	27.7135	34.1047	17	3.7	330	65	−35	8.85E+20
24	41070	0.504977	27.6992	34.0852	16	3.6	218	56	−97	6.25E+20
25	41371	0.665289	27.6899	34.0754	17	4.2	175	70	65	5.04E+21
26	41713	0.49853	27.8517	34.6574	12	3.9	340	60	45	1.77E+21
27	41436	0.512269	26.4802	34.7757	14	3.3	290	80	100	2.2E+20
28	41928	0.904595	26.7635	34.7941	13	4	344	78	−144	2.51E+21
29	42288	0.459144	26.9813	34.9087	12	3.8	55	65	−30	1.25E+21
30	43998	0.604167	27.17	34.75	10	5.5	139	76	−133	4.62E+23
31	45030	0.998611	27.5	34.13	19	4.5	235	49	−95	1.43E+22

the moment-magnitude scaling relation. They are not independent fitted parameters and should not be confused with the lower-case Gutenberg-Richter coefficients a and b. The auxiliary terms are calculated as:

$$A = 10^{[a+(bd/c)]} \text{ and } B = {}^{b}\!/_{c} \tag{4}$$

where a and b are the constants of the Gutenberg–Richter law

$$log_{10}N = a - bM \tag{5}$$

and the moment–magnitude scaling relation

$$log_{10}M_o = cM_w + d \tag{6}$$

with c = 1.5 and d = 9.1 (Hanks and Kanamori 1979). Parameters a and b are listed in Table 1. Following Kostrov's relation, the seismic strain-rate tensor is expressed as:

$$\dot{\varepsilon}_{ij} = \frac{1}{2\mu V}\dot{M}_o\overline{M}_{ij} i,j = 1,2,3 \tag{7}$$

where μ is the shear modulus, and V is the effective seismogenic volume, defined as the product of the active crustal thickness and planform area. The dimensionless tensor ($\overline{M}_{ij}$) represents the normalized deformation geometry derived from focal mechanisms (Aki & Richards 1980), as represented in Eq. 1 in terms of (strike ϕ, dip δ, and rake λ). Following Jackson and McKenzie (1988), the velocity tensor components are calculated as:

$$\begin{aligned}
\dot{u}_{xx} &= \frac{\dot{M}_o.\overline{M}_{xx}}{2\mu.A_{xz}} \\
\dot{u}_{yy} &= \frac{\dot{M}_o.\overline{M}_{yy}}{2\mu.A_{yz}} \\
\dot{u}_{zz} &= \frac{\dot{M}_o.\overline{M}_{zz}}{2\mu.A_{xy}} \\
\dot{u}_{xy} = \dot{u}_{yx} &= \frac{\dot{M}_o.\overline{M}_{xy}}{\mu.A_{yz}} \\
\dot{u}_{xz} = \dot{u}_{zx} &= \frac{\dot{M}_o.\overline{M}_{xz}}{\mu.A_{xy}} \\
\dot{u}_{yz} = \dot{u}_{zy} &= \frac{\dot{M}_o.\overline{M}_{yz}}{\mu.A_{xy}}
\end{aligned} \tag{8}$$

In these expressions, A_{xz}, A_{yz}, and A_{xy} denote the cross-sectional areas in the respective planes. The diagonal terms $\dot{u}_{xx}, \dot{u}_{yy}, and \dot{u}_{zz}$ indicate extension or contraction rates along the principal axes, while the off-diagonal terms $\dot{u}_{xy}, \dot{u}_{xz}, and \dot{u}_{yz}$ represent shear deformation. The eigenvectors of the moment tensor define the principal deformation axes (P, T, B), which in turn characterize the style of faulting in the region. This methodological approach provides a consistent and reproducible basis for quantifying seismic deformation in the Northern Red Sea rift system.

Uncertainties are propagated by jointly sampling bootstrap realizations of the focal-mechanism parameters in Eq. 1 and, where applicable, the shear modulus and seismogenic volume. Each realization yields a full tensor whose eigen-decomposition provides the principal strain rates and P-, T-, and B-axes. Posterior distributions are summarized using median values and 16th-84th percentile credible intervals. To assess epistemic uncertainty caused by focal-mechanism heterogeneity and finite sampling, we perform nonparametric bootstrap resampling of the focal-mechanism set in each zone. We use 10,000 bootstrap realizations because preliminary convergence tests showed that median tensor components, deviatoric norms, and principal-axis orientations stabilized by this sample size, whereas smaller ensembles produced less stable tails in the uncertainty distributions. For each bootstrap iteration:

Input mechanisms and locations are resampled with replacement.
Gaussian noise is added to the strike, dip, rake, and magnitude to reflect measurement uncertainty.
The average moment tensor, moment rate, strain rate, and velocity tensors are recomputed.
The ensemble of bootstrap realizations is compiled for statistical analysis.

From these ensembles, we compute the mean, standard deviation, median, and 95% confidence intervals for each tensor component and for the principal axes (eigenvalues and eigenvectors). The P-axis represents the direction of maximum compression (most negative eigenvalue), the T-axis corresponds to maximum extension (most positive eigenvalue), and the B-axis denotes the intermediate axis. The azimuth and plunge uncertainties of these axes are quantified from the bootstrap distributions.Bootstrap convergence was evaluated by tracking the stabilization of the median tensor components, principal-axis orientations, and deviatoric norms as the number of realizations increased. This check supports the interpretation that dominant deformation style is stable even where absolute amplitudes are weakly resolved.

For non-circular parameters (e.g., eigenvalues, plunges), Kernel Density Estimation (KDE) is applied to estimate the mode and 95% credible intervals. Using a Gaussian kernel, the probability density function (PDF) of each parameter is computed, and the mode corresponds to the PDF maximum. Confidence intervals are defined by integrating the PDF outward from the mode until 95% of the total probability mass is captured. For circular parameters (e.g., azimuths), circular statistics are employed. Azimuths are converted to radians, and the circular mean (θ) and standard deviation (σ) are calculated as:

$$\sigma = \sqrt{-2\ln R} \tag{9}$$

where R is the mean resultant length. The 95% confidence interval for azimuths is given by $\theta \pm 1.96\sigma$, wrapped within 0°–360° to maintain angular continuity.

Where event density permits, the seismic moment-rate field is spatially distributed across a grid using kernel density estimation of hypocenters, and the average moment tensor is computed for each grid cell, including bootstrap resampling at the cell level. This produces spatially continuous maps of deformation style, illustrated through rose diagrams or beachball symbols, and probabilistic principal strain-rate fields with uncertainty bands. The KDE bandwidth is selected using likelihood cross-validation to optimize the bias-variance trade-off. Finally, zone-integrated principal strain-rate components, including extensional, compressional, and shear terms, are compared with geodetic divergence and shear derived from regional GPS velocity fields (Castro-Perdomo et al. 2022). Because geodesy captures the total deformation field, any systematic under-recovery by the seismic results is interpreted as a seismic deficit, reflecting strain accommodated aseismically by processes such as magmatic intrusion, fault creep, or ductile lower-crustal flow (Reilinger et al. 2006).

3.2 Visualization of tensor estimates

The probabilistic tensor estimates for each tectonic domain are visualized in Figs. 3, 4, and 5 and summarized in Table 3 using a consistent seven-panel layout that illustrates the deviatoric moment tensor, strain-rate tensor, and velocity tensor. Panel (a) presents the principal eigenvalues (P, B, T) with bootstrap-derived 1σ error bars; panel (b) shows the corresponding azimuth and plunge of the principal axes; panel (c) displays the three-dimensional

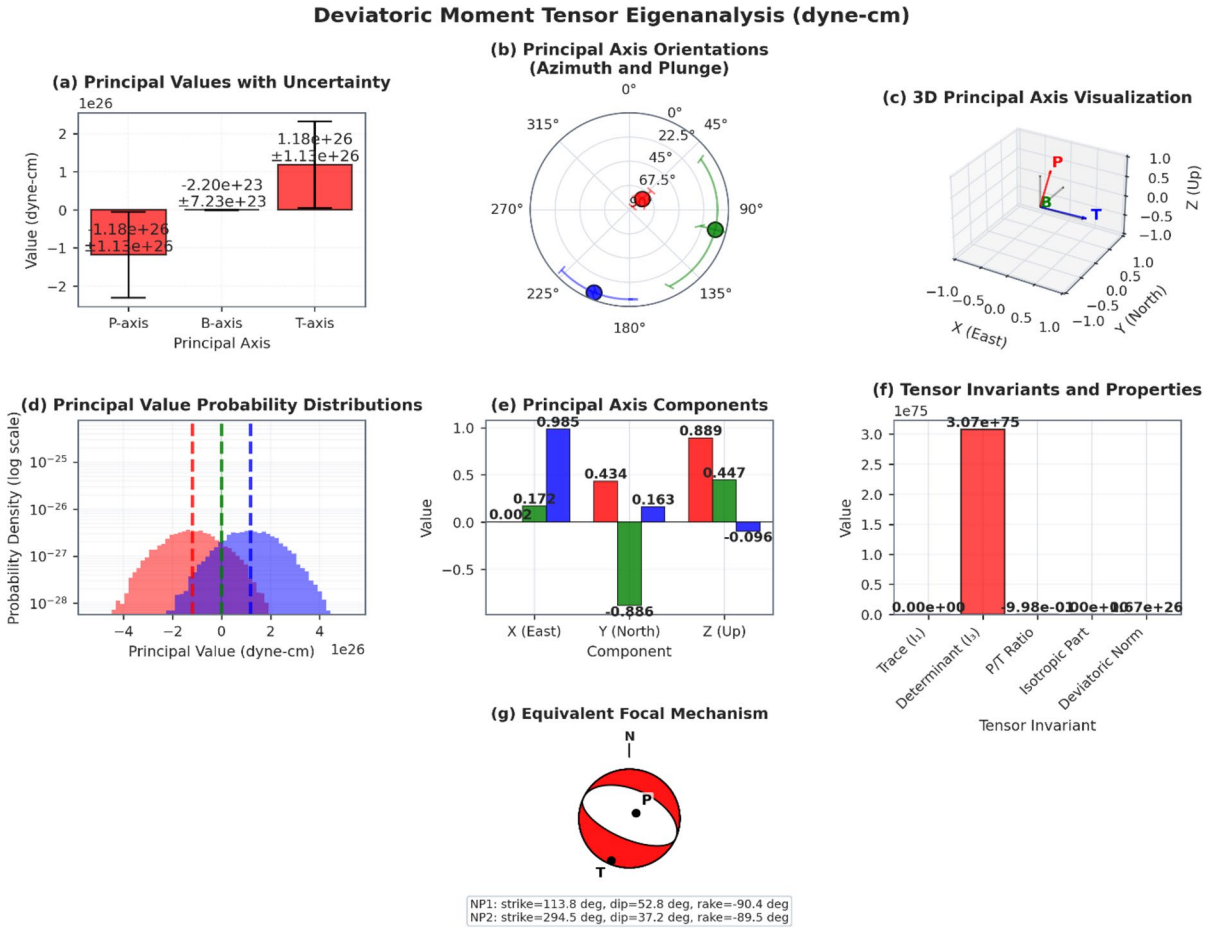


Fig. 3 a. Deviatoric moment tensor eigenanalysis for the Gulf of Suez region. (a Principal moment-tensor eigenvalues ($P(\lambda_1)$, $B(\lambda_2)$, $T(\lambda_3)$) with bootstrap-derived uncertainties (1σ). (b) Equal-area lower-hemisphere polar plot showing azimuth and plunge of principal axes; colors: red = P-axis, green = B-axis, blue = T-axis. (c) Three-dimensional representation of principal axes in East-North-Up coordinate frame; vector lengths scaled to eigenvalue magnitude. (d) Probability density functions of eigenvalues from bootstrap resampling (10,000 realizations). (e) Cartesian components (East, North, Up) of each principal axis. (f) Tensor invariants and derived properties: trace (I_1), determinant (I_3), isotropic component, P/T ratio, and deviatoric norm. Interpretation: Weak uniaxial extension consistent with a waning continental rift. (g) Beachball diagram showing the average focal mechanism obtained from moment tensor summation. **b**. Strain-rate tensor eigenanalysis for the Gulf of Suez region. (a) Principal strain-rate eigenvalues ($P(\lambda_1)$, $B(\lambda_2)$, $T(\lambda_3)$) with bootstrap-derived uncertainties (1σ). (b) Equal-area lower-hemisphere polar plot showing azimuth and plunge of principal axes; colors: red = P-axis, green = B-axis, blue = T-axis. (c) Three-dimensional representation of principal axes in East-North-Up coordinate frame; vector lengths scaled to eigenvalue magnitude. (d) Probability density functions of eigenvalues from bootstrap resampling (10,000 realizations). (e) Cartesian components (East, North, Up) of each principal axis. (f) Tensor invariants and derived properties: trace (I_1), determinant (I_3), isotropic component, P/T ratio, and deviatoric norm. Interpretation: Weak uniaxial extension consistent with a waning continental rift. (g) Beachball diagram showing the focal mechanism representing velocity tensor **c**. Velocity tensor eigenanalysis for the Gulf of Suez region. (a) Principal velocity eigenvalues ($P(\lambda_1)$, $B(\lambda_2)$, $T(\lambda_3)$) with bootstrap-derived uncertainties (1σ). (b) Equal-area lower-hemisphere polar plot showing azimuth and plunge of principal axes; colors: red = P-axis, green = B-axis, blue = T-axis. (c) Three-dimensional representation of principal axes in East-North-Up coordinate frame; vector lengths scaled to eigenvalue magnitude. (d) Probability density functions of eigenvalues from bootstrap resampling (10,000 realizations). (e) Cartesian components (East, North, Up) of each principal axis. (f) Tensor invariants and derived properties: trace (I_1), determinant (I_3), isotropic component, P/T ratio, and deviatoric norm. Interpretation: Weak uniaxial extension consistent with a waning continental rift. (g) Beachball diagram showing the focal mechanism representing velocity tensor

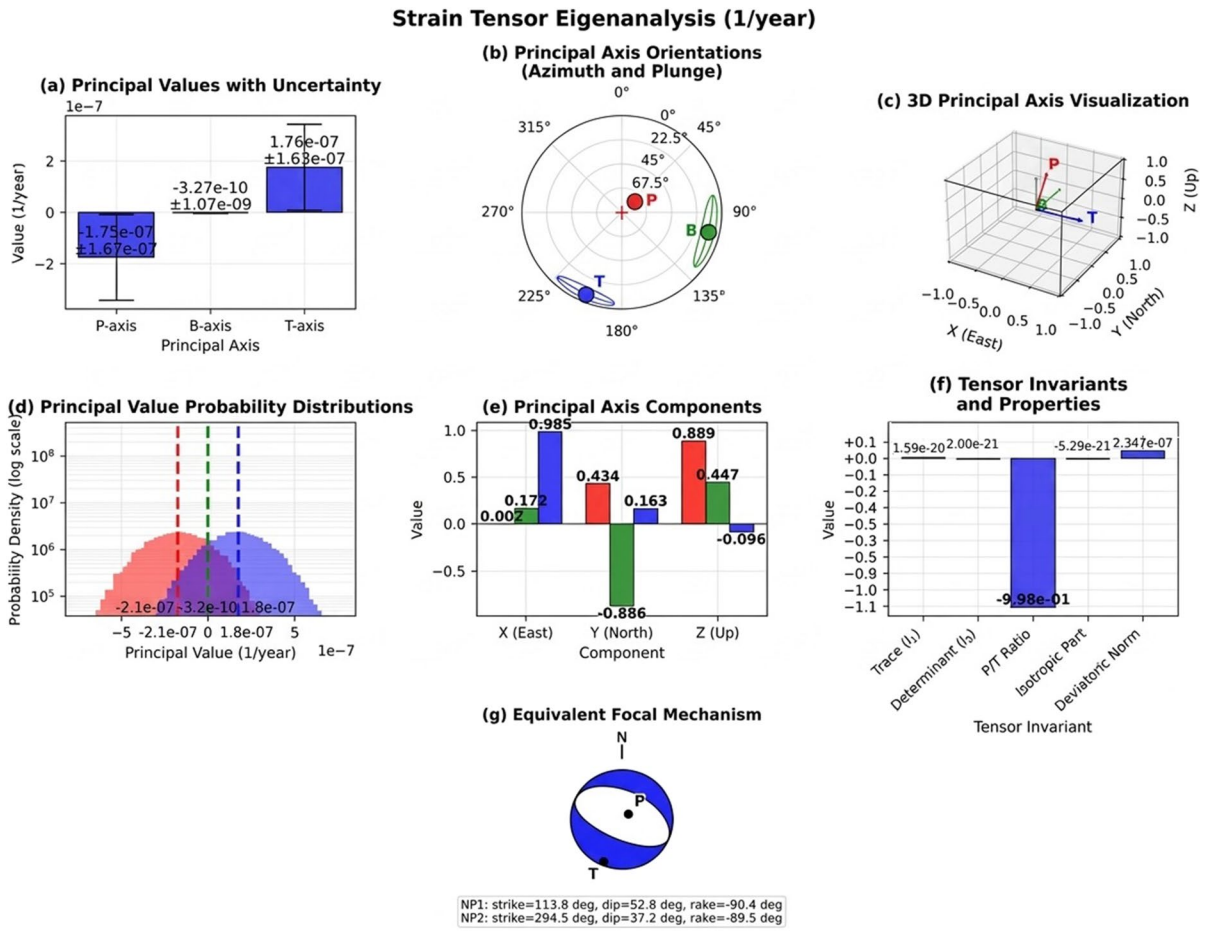


Fig. 3 (continued)

eigenvector geometry; panel (d) shows the bootstrap probability-density distributions; panel (e) reports principal-axis components; panel (f) summarizes tensor invariants; and panel (g) gives the equivalent double-couple focal mechanism with the P- and T-axis projections. This layout allows direct comparison between moment release, strain-rate geometry, and the model-equivalent velocity tensor.

4 Results and discussion

4.1 Gulf of Suez

The Gulf of Suez tensor solutions (Figs. 3a–c) indicate weak but well-defined present-day seismic deformation, consistent with a mature to waning rift system. The deviatoric moment tensor (Fig. 3a) returns principal eigenvalues of $P = -1.18 \times 10^{26} \pm 1.13 \times 10^{26}$ dyne·cm, $B = -2.20 \times 10^{23} \pm 7.23 \times 10^{23}$ dyne·cm, and $T = +1.18 \times 10^{26} \pm 1.13 \times 10^{26}$ dyne·cm in panel (a), where the near-zero intermediate eigenvalue and symmetric *P*–*T* pair are diagnostic of plane-strain deviatoric deformation, although the 1σ bootstrap error bars comparable to the mean values indicate that absolute amplitudes are weakly resolved. Panel (b) shows the *P*-axis at steep plunge near the centre of the polar projection, the *T*-axis at low plunge in the SW quadrant (~225°), and the *B*-axis sub-horizontal toward the ESE, the textbook signature of normal-fault kinematics, fully compatible with the rift-perpendicular extension expected for the Suez branch. The three-dimensional eigenvector

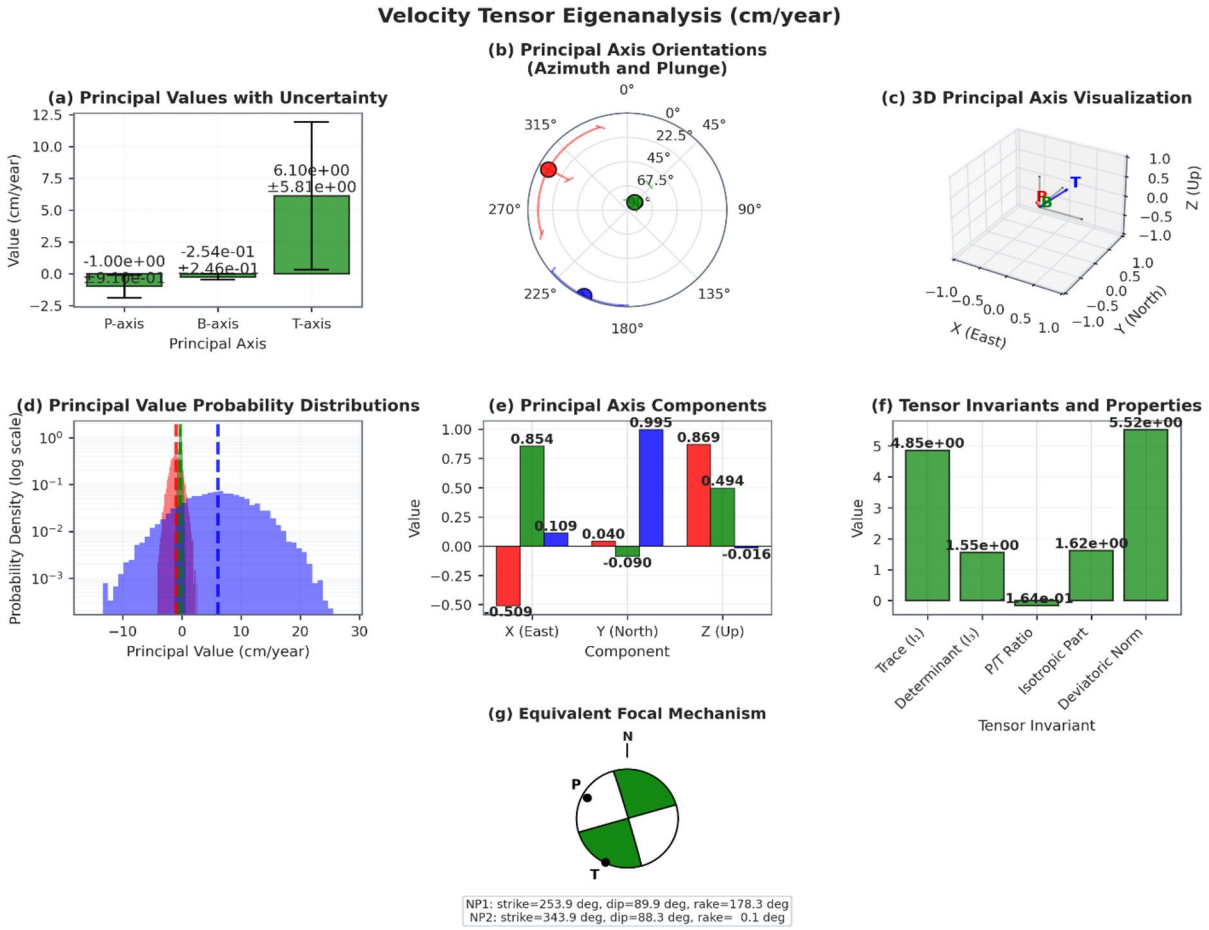


Fig. 3 (continued)

geometry in panel (c) confirms a near-vertical *P*-axis paired with a sub-horizontal *T*-axis lying close to the East–North plane, ruling out a substantial component of strike-slip or out-of-plane shear. The bootstrap probability-density distributions in panel (d) show the negative (*P*) and positive (*T*) branches separated by the central *B* peak at zero, but with substantial overlap near the origin — the most direct probabilistic expression of the waning-rift interpretation, since the deformation tensor is statistically distinguishable from zero only marginally at the 1σ level. Panel (e) returns a dominant Z-component for *P* (+0.889) and a dominant Y-component for *T* (+0.985), quantitatively confirming the normal-faulting geometry, while panel (f) yields a trace statistically indistinguishable from zero, a *P*/*T* ratio near unity (~0.998), and a deviatoric norm of ~ 1.67×10^{26} that quantifies the absolute size of the strain-energy budget. The equivalent double-couple focal mechanism in panel (g) is a near-pure normal-faulting solution (NP1: 113.8°/52.8°/−90.4°; NP2: 294.5°/37.2°/−89.5°), with rakes essentially at −90° on both nodal planes and no significant strike-slip component, compatible with the dominant style of moderate-magnitude earthquakes recorded historically in the Gulf of Suez (e.g., Morsy et al. 2011; Badreldin et al. 2019) and validating the PMTS solution against the empirical focal-mechanism population.

The strain-rate tensor (Fig. 3b) yields $P = -1.75 \times 10^{-7} \pm 1.67 \times 10^{-7}$ yr^{-1}, $B = -3.27 \times 10^{-10} \pm 1.07 \times 10^{-9}$ yr^{-1}, and $T = +1.76 \times 10^{-7} \pm 1.68 \times 10^{-7}$ yr^{-1} in panel (a), an amplitude consistent with a mature to waning rift rather than an actively extending segment. The principal-axis orientations and

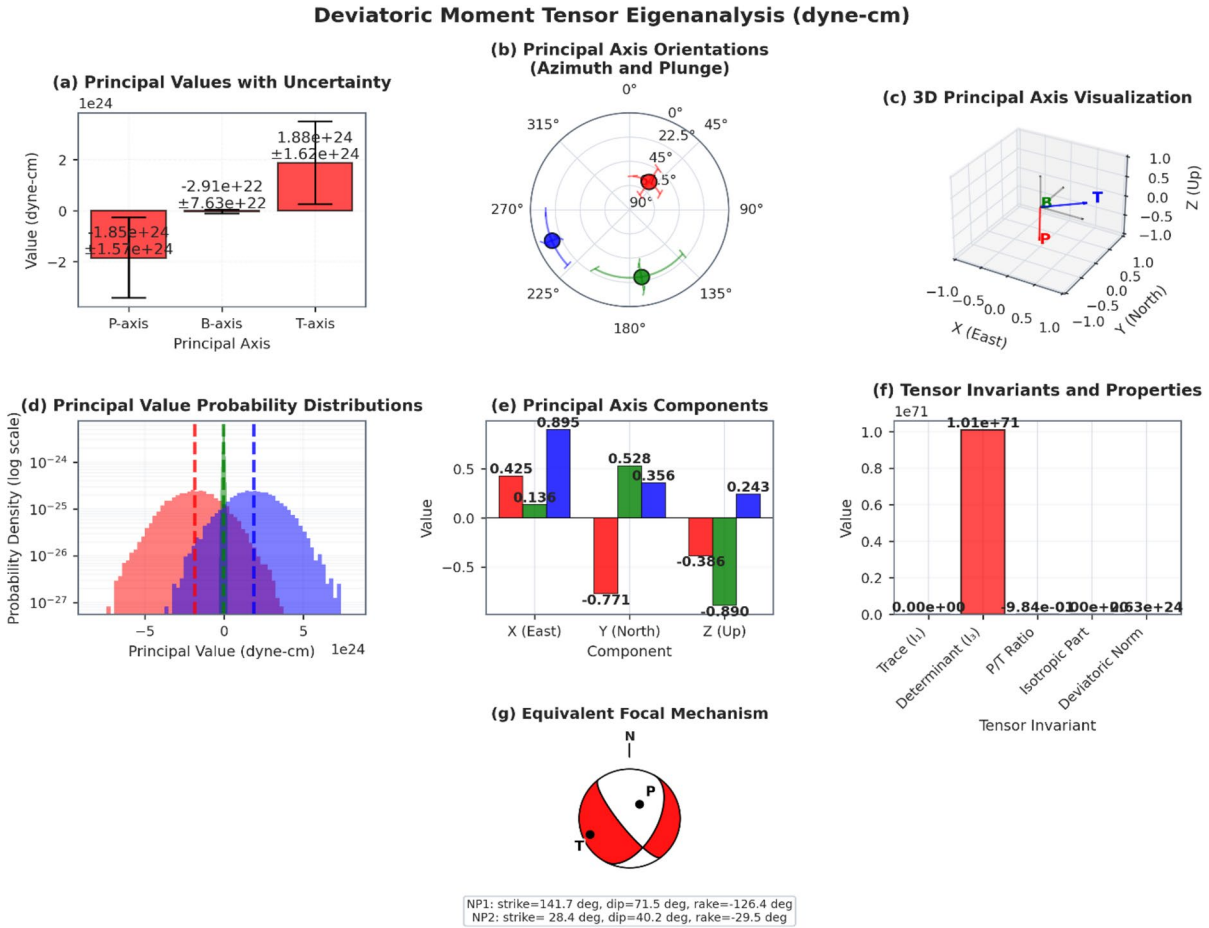


Fig. 4 a. Deviatoric moment tensor eigenanalysis for the northern Red Sea region. (a) Principal moment-tensor eigenvalues ($P(\lambda_1)$, $B(\lambda_2)$, $T(\lambda_3)$) with bootstrap-derived uncertainties (1σ). (b) Equal-area lower-hemisphere polar plot showing azimuth and plunge of principal axes; colors: red = P-axis, green = B-axis, blue = T-axis. (c) Three-dimensional representation of principal axes in East-North-Up coordinate frame; vector lengths scaled to eigenvalue magnitude. (d) Probability density functions of eigenvalues from bootstrap resampling (10,000 realizations). (e) Cartesian components (East, North, Up) of each principal axis. (f) Tensor invariants and derived properties: trace (I_1), determinant (I_3), isotropic component, P/T ratio, and deviatoric norm. Interpretation: Very low-amplitude oblique extension consistent with weak seismic coupling, heterogeneous rift deformation, and possible aseismic or magmatic accommodation. (g) Beachball diagram showing the average focal mechanism obtained from moment tensor summation. **b**. Strain-rate tensor eigenanalysis for the northern Red Sea region. (a) Principal strain-rate eigenvalues ($P(\lambda_1)$, $B(\lambda_2)$, $T(\lambda_3)$) with bootstrap-derived uncertainties (1σ). (b) Equal-area lower-hemisphere polar plot showing azimuth and plunge of principal axes; colors: red = P-axis, green = B-axis, blue = T-axis. (c) Three-dimensional representation of principal axes in East-North-Up coordinate frame; vector lengths scaled to eigenvalue magnitude. (d) Probability density functions of eigenvalues from bootstrap resampling (10,000 realizations). (e) Cartesian components (East, North, Up) of each principal axis. (f) Tensor invariants and derived properties: trace (I_1), determinant (I_3), isotropic component, P/T ratio, and deviatoric norm. Interpretation: Very low-amplitude oblique extension consistent with weak seismic coupling, heterogeneous rift deformation, and possible aseismic or magmatic accommodation. (g) Beachball diagram showing the focal mechanism representing velocity tensor

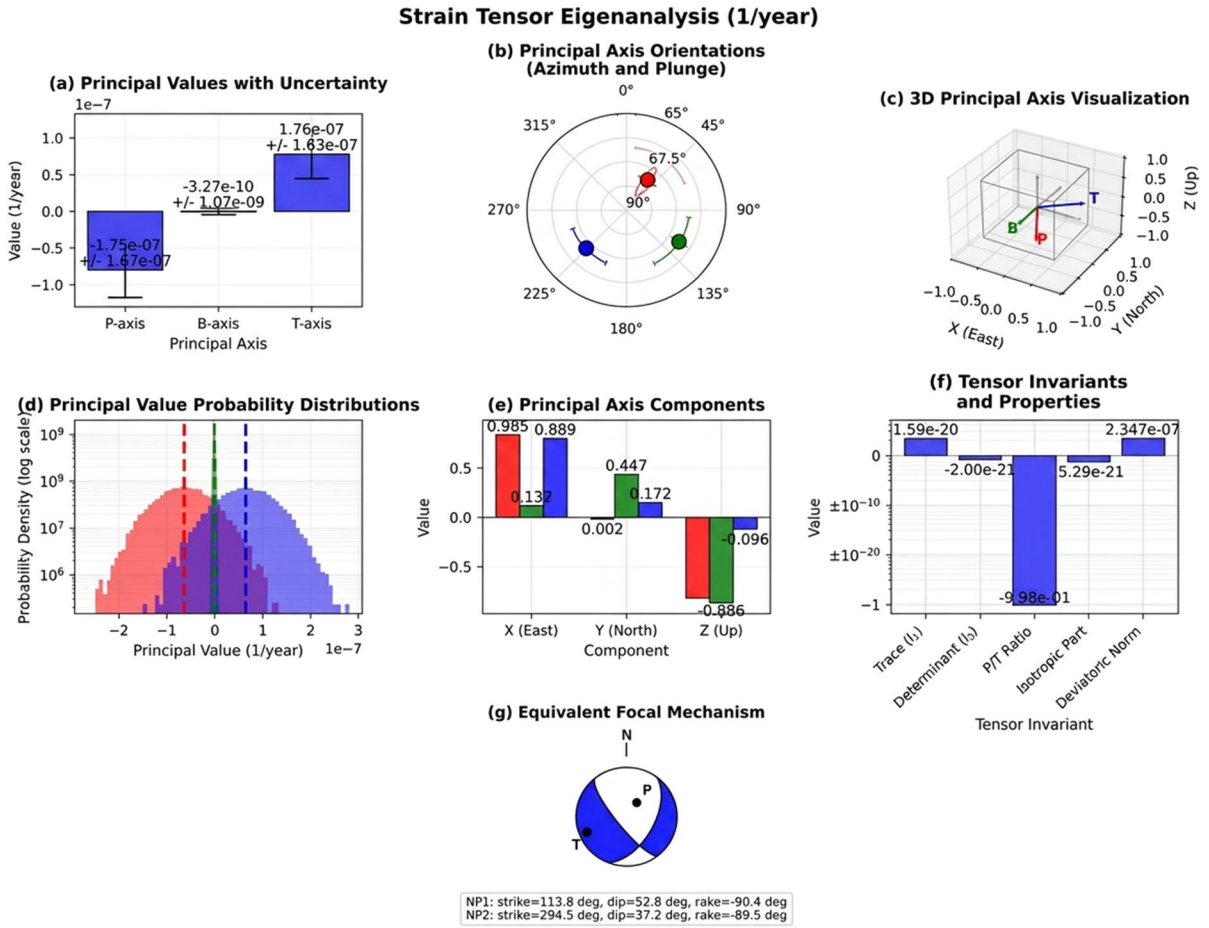


Fig. 4 (continued)

3D eigenvector geometry in panels (b) and (c) are identical in form to those of the moment tensor, as expected because the strain-rate tensor in PMTS is proportional to the cumulative moment tensor; the *T*-axis remains sub-horizontal toward the SW (~225°) and the *P*-axis sub-vertical. The bootstrap probability-density distributions in panel (d) again show pronounced overlap of the *P* and *T* branches across zero, the Cartesian components in panel (e) mirror those of the moment tensor, and the invariants in panel (f) confirm a deviatoric, plane-strain character with a near-unity *P*/*T* ratio (−0.998), a zero isotropic component, and a deviatoric norm of ~ 2.5×10^{-7} yr^{-1} as a single scalar measure of strain-rate magnitude. Panel (g) reproduces the same near-pure normal-faulting solution as the moment tensor, confirming a coherent extensional kinematic style.

The velocity tensor (Fig. 3c) returns $P=-1.00\times10^{0}\pm9.10\times10^{-1}$ cm yr^{-1}, $B=-2.54\times10^{-1}\pm2.46\times10^{-1}$ cm yr^{-1}, and $T=+6.10\times10^{0}\pm5.81\times10^{0}$ cm yr^{-1} in panel (a), with a shallow T-axis at azimuth ~ 315° in panel (b) and bootstrap uncertainty comparable to the mean — so this velocity amplitude must be interpreted strictly as a model-equivalent tensor amplitude, not as a directly resolved geodetic opening rate or plate-motion velocity. The 3D geometry, principal-axis components, and tensor invariants in panels (c)–(f) reflect the dominance of horizontal motion over vertical motion, with a deviatoric norm of ~ 5.5×10^{0} cm yr^{-1} and a P/T ratio of −0.164 indicating that

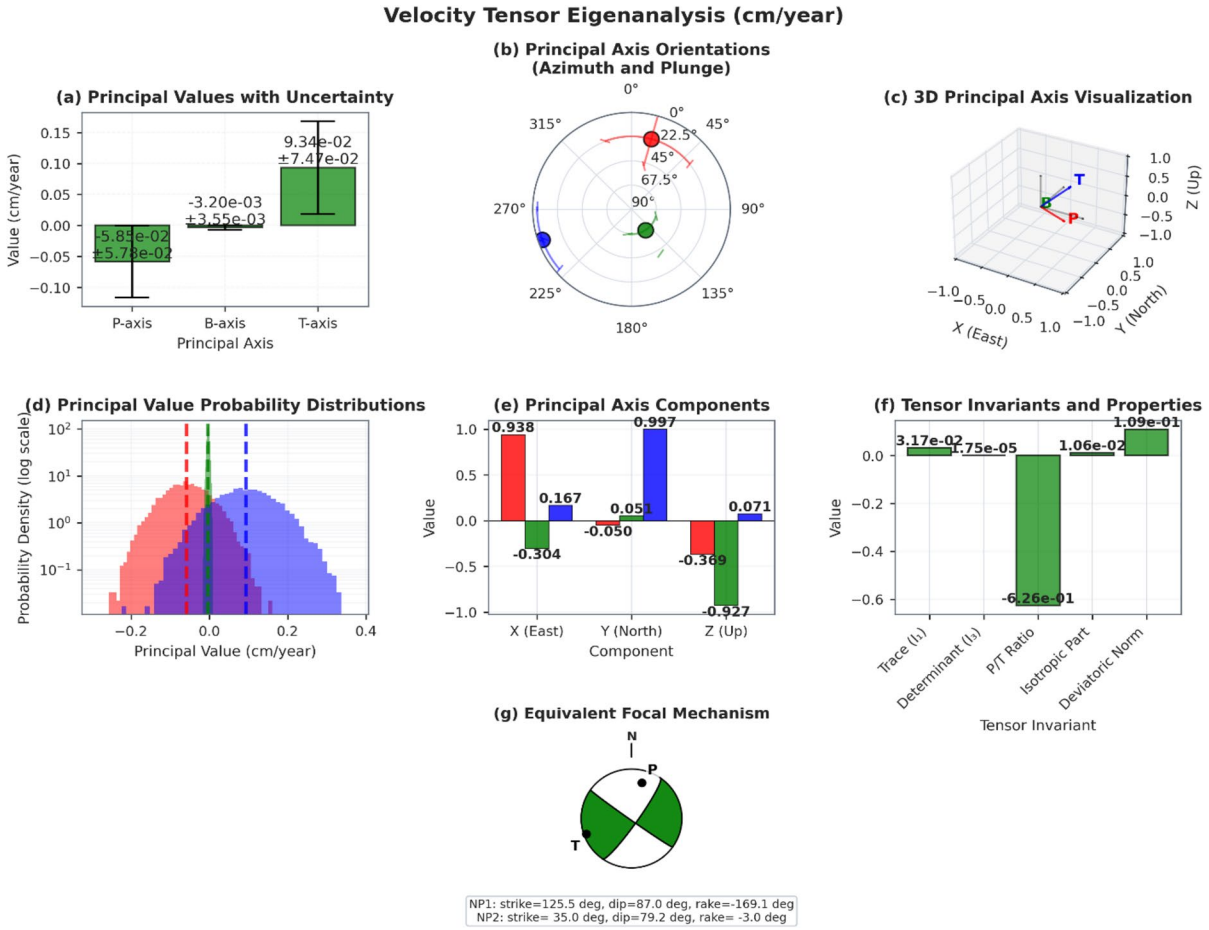


Fig. 4 (continued)

compressional and extensional velocity components are not balanced, a consequence of converting moment release to displacement under a finite source-volume assumption, which is the principal reason the velocity panel must be interpreted alongside the strain-rate and moment-tensor panels rather than in isolation. The equivalent focal mechanism in panel (g) of Fig. 3c (NP1: 253.9°/89.9°/178.3°; NP2: 343.9°/88.3°/0.1°) is dominated by near-vertical nodal planes with rakes near 0°/180°, indicating that the residual horizontal velocity field is dominated by strike-slip-like motion, in contrast to the pure normal-fault style of the strain-rate and moment tensors. Taken together, the integrated seven-panel diagnostic across the three tensor representations indicates continued but inefficient seismic deformation in the Gulf of Suez rather than a coherent and rapidly opening rift, with all three tensors consistently showing a normal-faulting style, sub-horizontal NE–SW extension, low absolute amplitudes, and bootstrap uncertainties comparable to the mean values — fully compatible with geodetic observations of very small present-day extension across the Gulf of Suez and supporting the waning-rift framework adopted in this study.

4.2 Northern Red Sea

The northern Red Sea axial rift (Figs. 4a–c) exhibits the lowest earthquake-derived deformation among the extensional domains analyzed here, with strain-rate amplitudes more than two orders of magnitude smaller than those of the Gulf of Aqaba. The deviatoric moment tensor (Fig. 4a) returns $P = -1.85 \times 10^{24} \pm 1.57 \times 10^{24}$ dyne·cm, $B = -2.91 \times 10^{22} \pm 7.63$

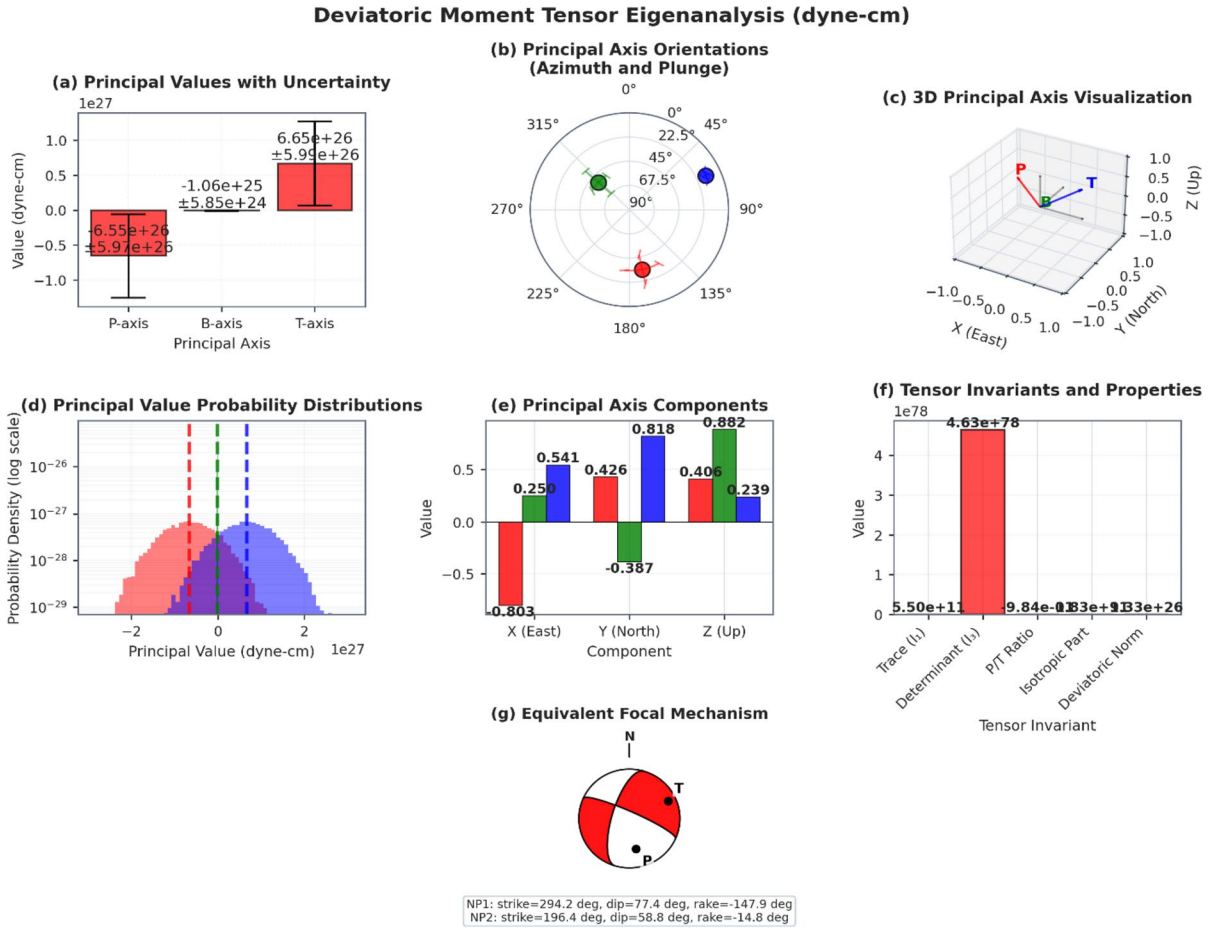


Fig. 5 a. Deviatoric moment tensor eigenanalysis for the Gulf of Aqaba region. (a) Principal moment-tensor eigenvalues ($P(\lambda_1)$, $B(\lambda_2)$, $T(\lambda_3)$) with bootstrap-derived uncertainties (1σ). (b) Equal-area lower-hemisphere polar plot showing azimuth and plunge of principal axes; colors: red = P-axis, green = B-axis, blue = T-axis. (c) Three-dimensional representation of principal axes in East-North-Up coordinate frame; vector lengths scaled to eigenvalue magnitude. (d) Probability density functions of eigenvalues from bootstrap resampling (10,000 realizations). (e) Cartesian components (East, North, Up) of each principal axis. (f) Tensor invariants and derived properties: trace (I_1), determinant (I_3), isotropic component, P/T ratio, and deviatoric norm. Interpretation: Strike-slip to transtensional deformation consistent with active localization along the Gulf of Aqaba–Dead Sea Transform. (g) Beachball diagram showing the average focal mechanism obtained from moment tensor summation. **b**. Strain-rate tensor eigenanalysis for the Gulf of Aqaba region. (a) Principal strain-rate eigenvalues ($P(\lambda_1)$, $B(\lambda_2)$, $T(\lambda_3)$) with bootstrap-derived uncertainties (1σ). (b) Equal-area lower-hemisphere polar plot showing azimuth and plunge of principal axes; colors: red = P-axis, green = B-axis, blue = T-axis. (c) Three-dimensional representation of principal axes in East-North-Up coordinate frame; vector lengths scaled to eigenvalue magnitude. (d) Probability density functions of eigenvalues from bootstrap resampling (10,000 realizations). (e) Cartesian components (East, North, Up) of each principal axis. (f) Tensor invariants and derived properties: trace (I_1), determinant (I_3), isotropic component, P/T ratio, and deviatoric norm. Interpretation: Strike-slip to transtensional deformation consistent with active localization along the Gulf of Aqaba–Dead Sea Transform. (g) Beachball diagram showing the focal mechanism representing velocity tensor

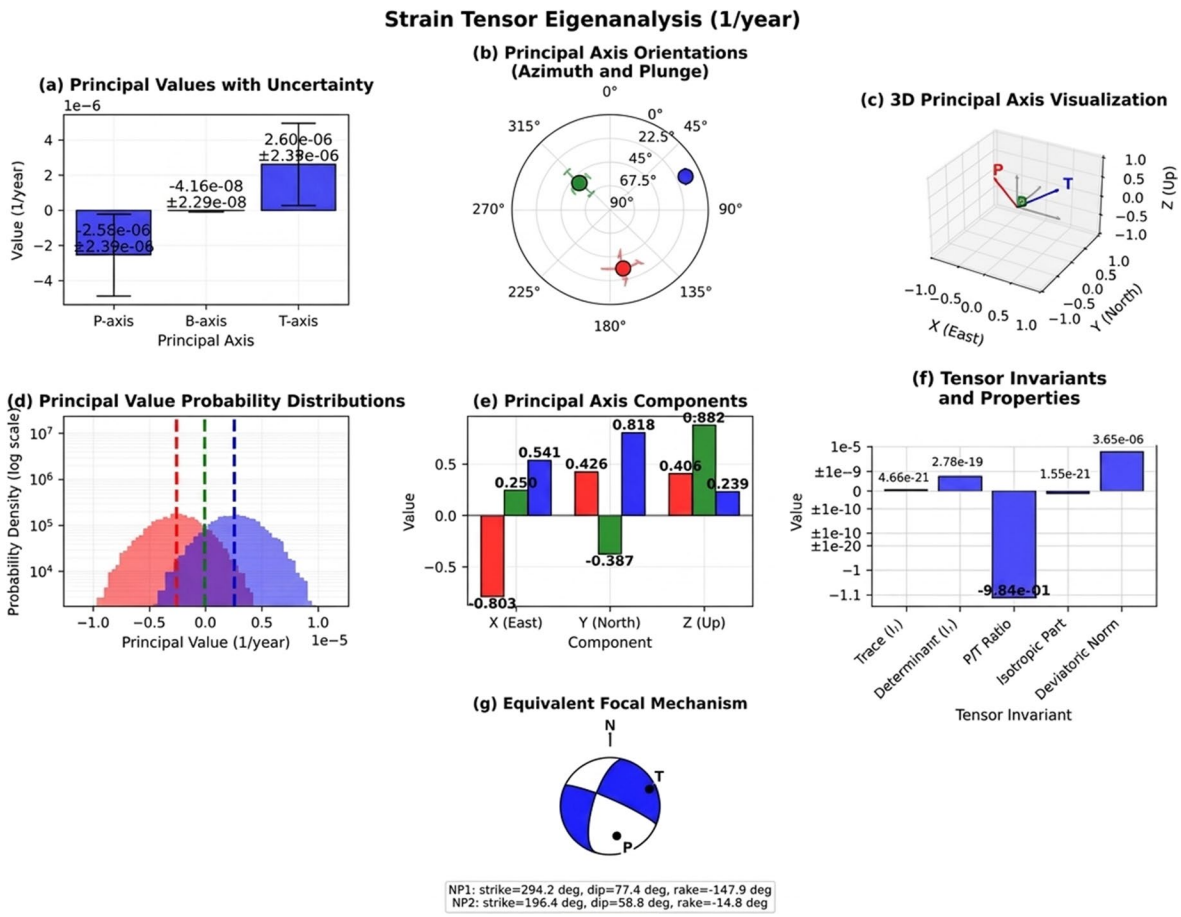


Fig. 5 (continued)

$\times 10^{22}$ dyne·cm, and $T = +1.88 \times 10^{24} \pm 1.62 \times 10^{24}$ dyne·cm in panel (a), almost two orders of magnitude smaller than the Gulf of Suez and four orders smaller than the Gulf of Aqaba, with 1σ error bars nearly equal to the means, so that the eigenvalues are statistically only marginally non-zero. Panel (b) shows the *P*-axis at moderate plunge near the centre, the *T*-axis at shallow plunge in the SW quadrant (~225°), and the *B*-axis at low plunge in the WSW quadrant (~250°), with bootstrap dispersion (red and blue arcs) markedly broader than for the Gulf of Suez, consistent with spatially heterogeneous focal mechanisms along the axial rift. The 3D eigenvector geometry in panel (c) reflects an oblique-extensional rather than purely planar configuration, with the *T*-axis projecting toward the East–North quadrant and the *P*-axis having a substantial vertical component but rotated away from pure vertical, indicating a component of oblique slip in addition to dip-slip extension. Panel (d) returns broad probability-density distributions with substantial overlap between the negative and positive branches, flatter than those of the Gulf of Suez, providing the strongest probabilistic argument that the axial rift is presently weakly coupled seismically. The Cartesian components in panel (e) confirm a mixed kinematic geometry, with the *T*-axis having dominant X (+0.895) and Y (+0.356) components indicating a sub-horizontal NE-trending extensional axis, and the *P*-axis having substantial X (+0.425), Y (−0.771), and Z (−0.386) components consistent with a steeply plunging compressional axis with an oblique component. The invariants in panel (f) confirm an

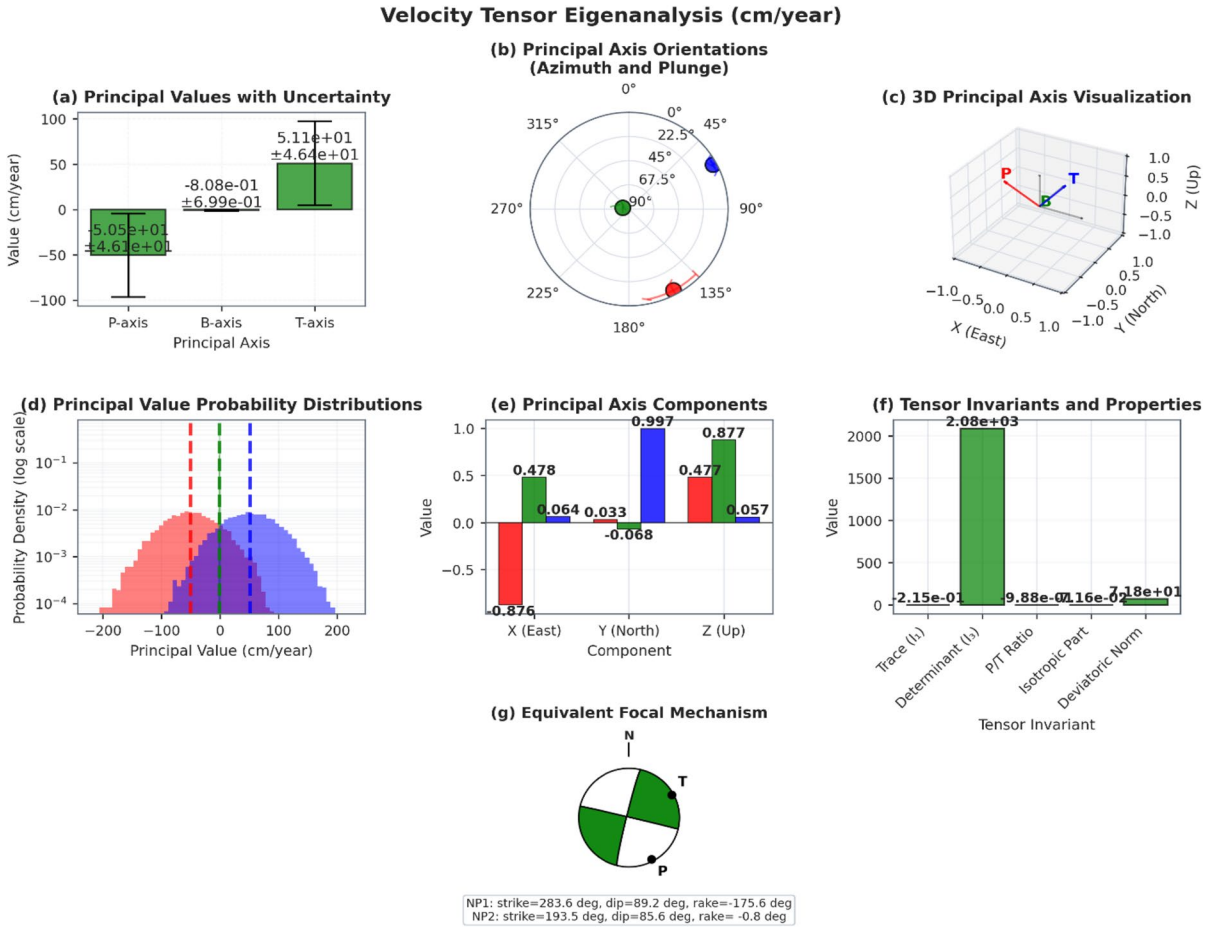


Fig. 5 (continued)

essentially zero trace, a determinant of 1.01×10^{71} (the smallest of the three sub-domains and a quantitative measure of the very low seismic strain energy released across the northern Red Sea), and a P/T ratio of -0.984, confirming an essentially balanced deviatoric tensor despite the low absolute amplitudes. The equivalent focal mechanism in panel (g) (NP1: 141.7°/71.5°/−126.4°; NP2: 28.4°/40.2°/−29.5°) is an oblique normal-faulting solution with a significant strike-slip component, with the −126.4° rake on NP1 corresponding to right-lateral oblique normal slip, a mixed kinematic style consistent with the structurally complex, distributed deformation observed in the axial rift, where multiple secondary faults accommodate part of the regional extension.

The strain-rate tensor (Fig. 4b) returns $P=-6.38\times10^{-9}\pm5.43\times10^{-9}$ yr^{-1}, $B=-1.01\times10^{-10}\pm2.64\times10^{-10}$ yr^{-1}, and $T=+6.48\times10^{-9}\pm5.59\times10^{-9}$ yr^{-1} in panel (a) — more than an order of magnitude lower than the Gulf of Suez and two orders lower than the Gulf of Aqaba, and panels (b)–(c) replicate the principal-axis orientations and 3D geometry of the moment tensor, with persistent broad bootstrap dispersion reaffirming the spatial heterogeneity of the deformation field. Panel (d) displays peaks centered very close to zero with substantial mutual overlap and the smallest eigenvalue amplitudes among the three sub-domains, reinforcing the conclusion of weak seismic coupling, while panels (e)–(f) confirm a deviatoric tensor (zero trace, P/T ratio of -0.984, deviatoric norm of $\sim9\times10^{-9}$ yr^{-1}, the smallest of the three sub-domains, providing the most direct quantitative measure of the very low seismic strain rate). Panel (g) is identical in form to the moment-tensor

Table 3 Eigensystem of the moment, strain-rate, and velocity tensors for the three seismogenic zones

Tensor	Axis	λ mean ± SD	φ mean ± SD (°)	δ mean ± SD (°)
Moment	P-axis	−6.547e+26 ± 5.970e+26	168.1 ± 33.0	33.3 ± 14.0
	B-axis	−1.064e+25 ± 5.855e+24	311.9 ± 29.1	52.1 ± 15.7
	T-axis	+6.653e+26 ± 5.987e+26	65.3 ± 8.2	13.7 ± 3.0
Strain-rate	P-axis	−2.562e-06 ± 2.336e-06	168.1 ± 33.0	33.3 ± 14.0
	B-axis	−4.162e-08 ± 2.291e-08	311.9 ± 29.1	52.1 ± 15.7
	T-axis	+2.604e-06 ± 2.343e-06	65.3 ± 8.2	13.7 ± 3.0
Velocity	P-axis	−5.050e+01 ± 4.608e+01	151.9 ± 34.1	4.3 ± 7.1
	B-axis	−8.079e-01 ± 6.989e-01	284.8 ± 27.4	84.2 ± 7.3
	T-axis	+5.109e+01 ± 4.641e+01	61.5 ± 9.8	3.2 ± 1.6
Gulf of Suez (mature to waning rift)				
Tensor	**Axis**	**λ mean ± SD**	**φ mean ± SD (°)**	**δ mean ± SD (°)**
Moment	P-axis	−1.181e+26 ± 1.128e+26	48.9 ± 48.2	74.9 ± 11.4
	B-axis	−2.202e+23 ± 7.233e+23	103.4 ± 99.0	10.0 ± 14.3
	T-axis	+1.183e+26 ± 1.131e+26	202.7 ± 49.8	6.7 ± 2.6
Strain-rate	P-axis	−1.752e-07 ± 1.675e-07	48.9 ± 48.2	74.9 ± 11.4
	B-axis	−3.267e-10 ± 1.073e-09	103.4 ± 99.0	10.0 ± 14.3
	T-axis	+1.755e-07 ± 1.678e-07	202.7 ± 49.8	6.7 ± 2.6
Velocity	P-axis	−1.000e+00 ± 9.097e-01	297.9 ± 88.9	9.2 ± 21.1
	B-axis	−2.536e-01 ± 2.465e-01	40.3 ± 69.6	80.4 ± 21.0
	T-axis	+6.105e+00 ± 5.814e+00	206.2 ± 48.0	1.0 ± 0.5
Northern Red Sea Rift (lowest seismic extension; transient or waning rift)				
Tensor	**Axis**	**λ mean ± SD**	**φ mean ± SD (°)**	**δ mean ± SD (°)**
Moment	P-axis	−1.846e+24 ± 1.572e+24	34.0 ± 57.2	58.8 ± 14.9
	B-axis	−2.911e+22 ± 7.629e+22	170.2 ± 79.6	26.8 ± 13.0
	T-axis	+1.876e+24 ± 1.618e+24	247.9 ± 41.0	13.7 ± 6.8
Strain-rate	P-axis	−6.381e-09 ± 5.431e-09	34.0 ± 57.2	58.8 ± 14.9
	B-axis	−1.006e-10 ± 2.636e-10	170.2 ± 79.6	26.8 ± 13.0
	T-axis	+6.482e-09 ± 5.592e-09	247.9 ± 41.0	13.7 ± 6.8
Velocity	P-axis	−5.845e-02 ± 5.777e-02	15.4 ± 72.4	22.1 ± 26.1
	B-axis	−3.204e-03 ± 3.547e-03	147.0 ± 83.0	66.8 ± 25.8
	T-axis	+9.336e-02 ± 7.469e-02	250.8 ± 42.1	4.0 ± 2.1

focal mechanism and reflects the same oblique normal-faulting style.

The velocity tensor (Fig. 4c) returns $P = -5.85 \times 10^{-2} \pm 5.78 \times 10^{-2}$ cm yr^{-1}, $B = -3.20 \times 10^{-3} \pm 3.55 \times 10^{-3}$ cm yr^{-1}, and $T = +9.34 \times 10^{-2} \pm 7.47 \times 10^{-2}$ cm yr^{-1} in panel (a), with a shallow T-axis (azimuth ~ 50°, plunge ~ 22.5° in panel b) compatible with extension along the WNW–ESE-trending axial rift and bootstrap arcs wider than in the Gulf of Aqaba, reflecting weaker localization. The 3D geometry, principal-axis components, and tensor invariants in panels (c)–(f) all return very small absolute values, with a deviatoric norm of ~ 1.1×10^{-1} cm yr^{-1}, a small but non-zero trace (3.17×10^{-2}), and a P/T ratio of −0.626 intermediate between the well-balanced strike-slip Aqaba tensor and the strongly imbalanced Suez velocity tensor. The equivalent focal mechanism in panel (g) (NP1: 125.5°/87.0°/−169.1°; NP2: 35.0°/79.2°/−3.0°) is dominated by sub-vertical strike-slip on rift-parallel and rift-perpendicular planes, again reflecting the cumulative horizontal motion implied by the velocity-tensor conversion rather than the instantaneous fault style. Taken together, the seven panels across the three tensor representations indicate that the northern Red Sea rift is presently characterized by low seismic-coupling efficiency, with the bulk of strain likely partitioned into aseismic dyking, magmatic and

thermomechanical weakening, and distributed small-magnitude faulting that lies below the catalog completeness threshold. The eastward offset of young rift-related magmatism, together with the predicted future jump of the extensional axis into Arabia (Artemieva et al. 2022), provides an independent geodynamic framework for interpreting this domain as a waning or transient rift segment rather than a fully mature spreading center (El Khrepy et al. 2021; Artemieva et al. 2022). As for the other regions, these values are treated as model-equivalent kinematic quantities derived from the seismic moment budget and not direct GPS-equivalent displacement rates.

4.3 Gulf of aqaba

The Gulf of Aqaba (Figs. 5a–c) shows the strongest and most coherent deformation signal among the three domains, with strain-rate amplitudes an order of magnitude greater than in the Gulf of Suez and two orders greater than in the northern Red Sea. The deviatoric moment tensor (Fig. 5a) returns $P = -6.55 \times 10^{26} \pm 5.97 \times 10^{26}$ dyne·cm, $B = -1.06 \times 10^{25} \pm 5.85 \times 10^{24}$ dyne·cm, and $T = +6.65 \times 10^{26} \pm 5.99 \times 10^{26}$ dyne·cm in panel (a), and although the 1σ error bars remain comparable to the mean values, the absolute amplitudes are an order of magnitude greater than in the Gulf of Suez and two orders greater than in the northern Red Sea, marking the Gulf of Aqaba as the most kinematically active of the three domains. Panel (b) plots both *P* (red, in the SE quadrant near 135°) and *T* (blue, in the NE quadrant near 45°) axes close to the perimeter of the polar projection, indicating sub-horizontal plunges, while the *B*-axis is plotted near the centre, indicating sub-vertical plunge, the canonical signature of strike-slip to transtensional deformation along a vertical fault system, consistent with the NNE–SSW orientation of the Dead Sea Transform. The 3D eigenvector geometry in panel (c) shows tightly clustered *P* and *T* eigenvectors confined to a near-horizontal plane with the *B*-eigenvector projecting close to vertical, diagnostic of pure to slightly transtensional strike-slip motion and confirming that deformation is concentrated on a vertical fault system rather than distributed across an oblique-extension zone. The bootstrap probability-density distributions in panel (d) are clearly bimodal with well-separated peaks for the negative (*P*) and positive (*T*) eigenvalue branches and only minor overlap near zero, the strongest probabilistic argument for active strain localization along the Aqaba transform. Panel (e) confirms two near-horizontal principal axes, the *P*-axis with dominant X (−0.803) and substantial Y (+0.426) and Z (+0.406) components, and the *T*-axis with dominant Y (+0.818) and subordinate X (+0.541) and Z (+0.239) components, and a near-vertical intermediate axis, consistent with strike-slip kinematics on a vertical fault. The invariants in panel (f) return an essentially zero trace, a determinant of 4.63×10^{78} (by far the largest of the three domains), and a *P*/*T* ratio of −0.984, together quantifying a high-amplitude, plane-strain, deviatoric deformation field, the kinematic fingerprint of an actively slipping transform boundary. The equivalent focal mechanism in panel (g) (NP1: 294.2°/77.4°/−147.9°; NP2: 196.4°/58.8°/−14.8°) is dominated by strike-slip motion with a minor normal component, and following standard convention for the Dead Sea Transform, the NNE-trending nodal plane (NP2) corresponds to left-lateral motion, consistent with the well-established left-lateral kinematics of the transform system.

The strain-rate tensor (Fig. 5b) returns $P = -2.56 \times 10^{-6} \pm 2.34 \times 10^{-6}$ yr^{-1}, $B = -4.16 \times 10^{-8} \pm 2.29 \times 10^{-8}$ yr^{-1}, and $T = +2.60 \times 10^{-6} \pm 2.34 \times 10^{-6}$ yr^{-1} in panel (a), an order of magnitude greater than in the Gulf of Suez and two orders greater than in the northern Red Sea, while panels (b)–(c) replicate the strike-slip principal-axis orientations and 3D eigenvector geometry of the moment tensor with bootstrap arcs tighter than in the other two sub-domains, reflecting a well-localized deformation field. Panel (d) shows bimodal distributions with well-separated peaks and only minor overlap near zero, providing strong statistical confidence in the resolved strain-rate tensor, and panels (e)–(f) reproduce the strike-slip geometry of the moment tensor and quantify a high-amplitude, plane-strain deviatoric field (zero trace, *P*/*T* ratio of −0.984, deviatoric norm of ~3.7×10^{-6} yr^{-1}). The equivalent focal mechanism in panel (g) is identical to that of the moment tensor and confirms strike-slip-dominated deformation.

The velocity tensor (Fig. 5c) is dominated by a nearly balanced compressional–extensional pair, with $P = -5.05 \times 10^{1} \pm 4.61 \times 10^{1}$ cm yr^{-1}, $B = -8.08 \times 10^{-1} \pm 6.99 \times 10^{-1}$ cm yr^{-1}, and

$T = +5.11 \times 10^{1} \pm 4.64 \times 10^{1}$ cm yr^{-1} in panel (a), and panel (b) shows shallow P and T plunges and a near-vertical B-axis. The large amplitude, yet substantial uncertainty, of this velocity tensor underscores that it should be interpreted as a model-equivalent quantity rather than as a one-to-one substitute for GPS-derived velocities; the strain-rate tensor is the preferred quantity for regional tectonic interpretation. The 3D geometry, principal-axis components, and tensor invariants in panels (c)–(f) confirm strike-slip kinematics, with a near-zero trace (-2.15×10^{-1}), a P/T ratio of -0.988, and a deviatoric norm of $\sim 7.18 \times 10^{1}$ cm yr^{-1} — values that confirm a high-amplitude, deviatoric, plane-strain velocity field consistent with the slipping Dead Sea Transform. The equivalent focal mechanism in panel (g) (NP1: 283.6°/89.2°/−175.6°; NP2: 193.5°/85.6°/−0.8°) is a near-pure strike-slip solution with vertical nodal planes and rakes near 0°/180°, with the NNE-trending plane (NP2) at strike 193.5° and rake −0.8° corresponding to essentially pure left-lateral motion on a vertical fault, the canonical kinematic signature of the Dead Sea Transform. Taken together, the integrated seven-panel diagnostic across the three tensor representations supports the interpretation that the Gulf of Aqaba is the most kinematically active sub-domain of the Sinai triple junction, dominated by strike-slip to transtensional deformation along the Dead Sea Transform; the Gulf of Aqaba should therefore not be characterized as a waning transform, and the waning-rift interpretation applies only to any residual rift-normal extensional component that has been transferred into, or overprinted by, the active transform-transtensional motion. As elsewhere, comparison with geodetic studies indicates that the brittle, earthquake-producing seismic budget captures only part of the total deformation, with the remainder accommodated aseismically through creep, distributed deformation, and post-seismic or lower-crustal relaxation. The Gulf of Aqaba interpretation is synthesized below in the regional strain-partitioning discussion to avoid repetition and to place the transform-dominated signal in the broader Sinai triple-junction framework.

4.4 Regional strain partitioning and aseismic processes

The seven-panel diagnostics across the three sub-domains demonstrate strong deformation partitioning across the Sinai triple junction (Table 4 and Figs. 3, 4, and5). Panels (a) and (d) collectively show that the Gulf of Suez is characterized by weak but measurable seismic strain ($\sim 10^{-7}$ yr^{-1}) accompanied by broad uncertainty; the northern Red Sea axial rift records still lower and more heterogeneous earthquake-derived extension ($\sim 10^{-9}$ yr^{-1}); and the Gulf of Aqaba exhibits the largest strike-slip to transtensional tensor amplitudes ($\sim 10^{-6}$ yr^{-1}) with the tightest bootstrap distributions. Panels (b), (c), and (g) jointly indicate that the deformation *style* transitions from pure normal faulting in Suez (rakes $\sim -90°$ on both nodal planes) to oblique normal-faulting in the northern Red Sea (rake −126.4° on NP1) to nearly pure strike-slip in Aqaba (rake −0.8° on NP2 of the velocity tensor), while panel (f) provides invariant-based confirmation that all three domains operate within a deviatoric, plane-strain regime (*P*/*T* ratios all close to −1.0). Figure 6 illustrates the kinematic evolution of the northern Red Sea region, showing the Gulf of Suez, the Gulf of Aqaba, and the northern Red Sea axial rift, representative focal mechanisms summarizing the dominant deformation style of each zone, and relative plate-motion vectors. This pattern requires a more nuanced interpretation than a simple northward progression from active Red Sea rifting to waning Suez rifting. Waning or strongly decelerated rifting must instead be considered for both the Gulf of Suez and the northern Red Sea, whereas the Gulf of Aqaba accommodates active transform localization that may absorb or overprint residual rift-normal extension. This interpretation is compatible with basin-analysis evidence for Middle Miocene reduction of Suez rifting, recent evidence for slow post-main-rift extension in Suez, and geodynamic models suggesting that the north-central Red Sea rift may ultimately be bypassed by an eastward jump of the extensional axis into Arabia (Richardson and Arthur 1988; Bosworth et al. 2005; Artemieva et al. 2022; Fernandez-Blanco et al., 2025).

The systematic discrepancy between seismic and geodetic strain rates (summarized in Table 5) indicates that the earthquake-derived strain budget captures only part of the total deformation across the Sinai triple junction. The approximate 60–80% aseismic range is therefore treated as a regional, literature-supported estimate based on seismic–geodetic comparison, not as a uniquely resolved partition from the present PMTS analysis alone. In the northern Red Sea and Gulf of Suez, this aseismic component is likely distributed among dyking, stable fault creep, and

Table 4 Summary of probabilistic velocity tensor parameters and deformation regime derived from moment-tensor summation and bootstrap uncertainty

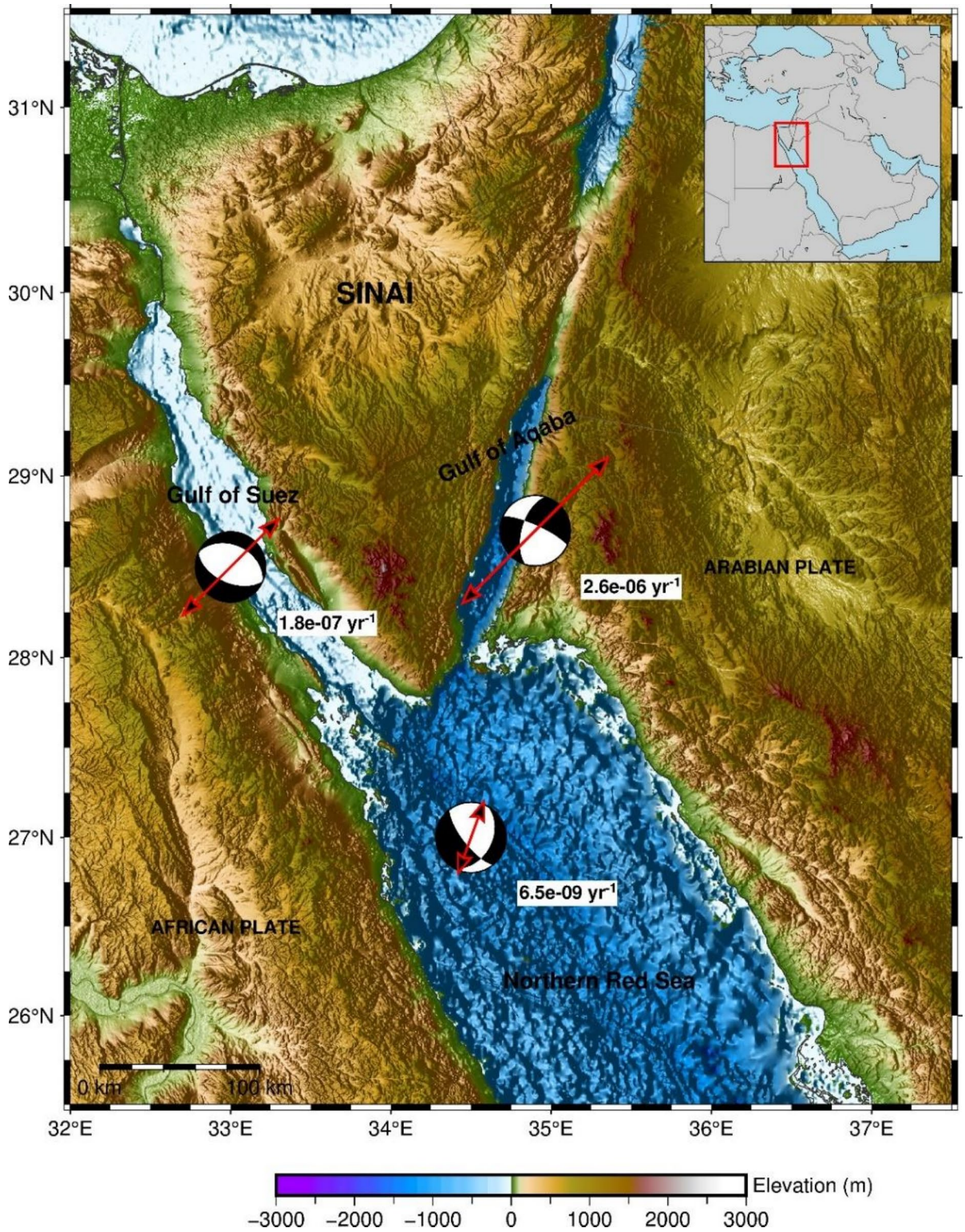
Parameter	Gulf of Suez (waning rift)	Northern Red Sea Rift (waning rift)	Gulf of Aqaba (transtension)
P-axis (σ_1/λ_1, max compression)	−1.000e+00 ± 9.097e-01	−5.845e-02 ± 5.777e-02	−5.050e+01 ± 4.608e+01
B-axis (σ_2/λ_2, intermediate)	−2.536e-01 ± 2.465e-01	−3.204e-03 ± 3.547e-03	−8.079e-01 ± 6.989e-01
T-axis (σ_3/λ_3, max extension)	+6.105e+00 ± 5.814e+00	+9.336e-02 ± 7.469e-02	+5.109e+01 ± 4.641e+01
P-axis (azimuth/plunge)	297.9 ± 88.9/9.2 ± 21.1	15.4 ± 72.4/22.1 ± 26.1	151.9 ± 34.1/4.3 ± 7.1
B-axis (azimuth/plunge)	40.3 ± 69.6/80.4 ± 21.0	147.0 ± 83.0/66.8 ± 25.8	284.8 ± 27.4/84.2 ± 7.3
T-axis (azimuth/plunge)	206.2 ± 48.0/1.0 ± 0.5	250.8 ± 42.1/4.0 ± 2.1	61.5 ± 9.8/3.2 ± 1.6
Trace (I_1)	≈ +4.85 (model-equivalent)	≈ $+3.17\times10^{-2}$	≈ -2.2×10^{-1}
Isotropic component ($I_1/3$)	≈ +1.62	≈ $+1.06\times10^{-2}$	≈ -7.4×10^{-2}
Deviatoric norm	≈ 6.2 (large uncertainty)	≈ 0.11	≈ 72
P/T ratio = (λ_1/λ_3)	≈ −0.16	≈ −0.63	≈ −0.99
Deformation regime	Weak, uncertain extension (waning rift)	Moderate, heterogeneous extension	Strong strike-slip to transtension
Qualitative seismic-geodetic deficit	Substantial deficit; likely creep, distributed deformation, or thermal/lower-crustal relaxation	Very large deficit; likely magmatic/dyking and lower-crustal or distributed deformation	Partial deficit; likely creep, post-seismic relaxation, and lower-crustal relaxation
Bootstrap uncertainty signature	Low dispersion for P- and B-axes; modest T-axis spread → reflects intrinsically low strain rate	Broad probability density functions for P- and T-axes → genuine spatial heterogeneity	Large P-axis dispersion → localized compression at step-overs; stable B-axis

viscoplastic lower-crustal flow; however, the present dataset cannot quantitatively separate these mechanisms. The very low seismic deformation observed in the northern Red Sea, despite its position along the rift axis, reinforces the inference that rift-related deformation there is either weakly coupled seismically, partly accommodated by magmatic and aseismic processes, or progressively transferred toward lithospheric weakness zones in western Arabia, as proposed by Artemieva et al. (2022).

4.5 Comparison with other triple junctions

The Sinai triple junction shares several kinematic features with other diffuse plate-boundary systems, yet it also exhibits distinctions that reflect its specific tectonic setting. The Afar Triple Junction provides the most direct analogue: an archetypal rift–rift–rift system linking the Red Sea, the Gulf of Aden, and the East African Rift, where extension is accommodated through dyking, faulting, and magmatic accretion (Hofstetter and Beyth 2003; Wright et al. 2006). A similar mode of partly aseismic, magmatically assisted extension may operate beneath the northern Red Sea, helping to explain its low earthquake-derived deformation. Unlike Sinai, however, Afar lacks a fully developed transform arm equivalent to the Dead Sea Transform, and strain is distributed more symmetrically among its three rift branches. The Azores Triple Junction offers a second analogue, combining extension and strike-slip deformation in a ridge–ridge–fault configuration, although its extensional strain is distributed more uniformly than in the northern Red Sea (Luis and Miranda 2008). The Mendocino Triple Junction is similarly instructive because of its transform component, but its compressional subduction setting differs fundamentally from the extensional–transtensional regime at Sinai (Furlong and Schwartz 2004).

A key characteristic of the Sinai triple junction is the coexistence of three contrasting tectonic elements: a mature to waning Gulf of Suez rift that preserves rift morphology but exhibits weak present-day strain; a northern Red Sea axial domain with even lower earthquake-derived deformation and pronounced spatial heterogeneity; and a transform boundary along the


SINAI
Gulf of Suez
Gulf of Aqaba
ARABIAN PLATE
AFRICAN PLATE
Northern Red Sea
1.8e-07 yr-1
2.6e-06 yr-1
6.5e-09 yr-1
0 km
100 km
31°N
30°N
29°N
28°N
27°N
26°N
32°E
33°E
34°E
35°E
36°E
37°E
Elevation (m)
−3000
−2000
−1000
0
1000
2000
3000

◂**Fig. 6** Synoptic kinematic model of the Sinai triple junction summarizing the main findings of this study. Three tectonic sub-domains, the Gulf of Suez, the northern Red Sea axial rift, and the Gulf of Aqaba, are delineated according to the spatial distribution of focal mechanisms analyzed using PMTS. At the centroid of each sub-domain, the representative double-couple beach-ball solution (derived from panel g in Figs. 3–5) illustrates the prevailing deformation regime: pure normal faulting in the Gulf of Suez, oblique normal faulting in the northern Red Sea, and left-lateral strike-slip faulting along the Gulf of Aqaba. Red arrows indicate the horizontal deformation-axis orientations inferred from the PMTS results (T-axes directed outward and P-axes inward), which are used here as kinematic stress-orientation proxies rather than as a formal stress inversion. The corresponding strain-rate values are also annotated

Gulf of Aqaba that accommodates active transtension rather than pure strike-slip motion. This configuration reflects oblique Arabia–Nubia divergence, which partitions deformation into both extension and shear, while inherited structural weaknesses and the evolving plate-boundary geometry have rendered parts of the older Red Sea–Suez rift system weakly active or effectively aseismic. The probabilistic framework adopted here by explicitly propagating uncertainties in focal-mechanism geometry and seismicity statistics, provides a robust means of distinguishing intrinsic tectonic variability from methodological uncertainty, and offers a transferable approach for analyzing deformation across other diffuse plate boundaries.

4.6 Comparison with independent stress-regime inversions

Independent validation of our PMTS kinematic results comes from several published stress tensor inversions based on well-constrained earthquake focal mechanisms. Using a comprehensive catalog of 234 events, Ali and Badreldin (2019) identified distinct present-day stress fields across Egypt, including an extensional regime characterized by NE–SW-oriented horizontal σ_3 in the Gulf of Suez, a strike-slip regime in the Gulf of Aqaba with the maximum compressive stress (σ_1) oriented NNW–SSE and the minimum compressive stress (σ_3) oriented ENE–WSW, and a predominantly tensional stress regime with subhorizontal σ_3 in the northern Red Sea region. Hussein et al. (2013) and Badawy (2005) independently confirm these patterns, showing normal-faulting with NE-SW extension in the Gulf of Suez and northern Red Sea, respectively, while Almadani (2020) further resolve strike-slip to transtensional conditions along the Gulf of Aqaba with local extensional overprints near the Dakar basin. The convergence between these independent stress inversions and our PMTS-derived P-, T-, and B-axis orientations robustly supports the conclusion that the three arms of the Sinai triple junction are characterized by fundamentally different tectonic regimes: extensional (waning rift) in the Gulf of Suez and northern Red Sea versus strike-slip/transtensional in the Gulf of Aqaba. We did not perform a separate formal stress inversion because that would require additional assumptions about fault friction, pore-fluid pressure, and slip tendency; instead, the independent published inversions provide an external check on the PMTS-derived deformation axes.

5 Conclusions

We present a probabilistic assessment of present-day crustal deformation using seismic moment-tensor summation with bootstrap uncertainty analysis across three distinct zones: The Gulf of Suez, the northern Red Sea axial rift, and the Gulf of Aqaba. The results reveal weak but measurable extension in the Gulf of Suez, even lower and more heterogeneous deformation in the northern Red Sea, and dominant strike-slip to transtensional kinematics in the Gulf of Aqaba. These findings imply a regional transition toward strongly decelerated rifting in the first two domains while active deformation localizes along the Aqaba–Dead Sea Transform, consistent with the hypothesis that the north-central Red Sea rift may be transient and future extension could migrate eastward into the Arabian shield.

We interpret the Gulf of Suez and northern Red Sea not as inactive, but as waning branches of the Red Sea–Suez system. Major subsidence and rift opening decreased sharply after the Middle Miocene as plate motion transferred to the Dead Sea Transform; the anomalously low seismic deformation in the northern Red Sea further suggests that a substantial component of strain there is probably aseismic or weakly seismic, accommodated by some combination of dyking/magmatic intrusion, distributed small-magnitude faulting, stable creep, and lower-crustal flow. The Gulf of Aqaba, by contrast, remains actively deforming, though its rift-normal component may reflect the progressive redistribution of earlier Red Sea–Suez extension. Residual strain in the waning rifts is partitioned

Table 5 Compact qualitative comparison between PMTS-derived seismic strain-rate scales and published geodetic constraints. The table is intended to support the seismic–geodetic deficit interpretation while avoiding a direct quantitative partition among dyking, creep, and lower-crustal flow, which is beyond the resolution of the present dataset

Domain	PMTS seismic strain-rate scale	Published geodetic constraint used for comparison	Interpretation of seismic–geodetic deficit	Key limitation
Gulf of Suez	~10^{-7} yr^{-1}	Regional GPS studies indicate only slow present-day extension across the Suez branch (McClusky et al. 2003; Reilinger et al. 2006; ArRajehi et al. 2010)	Weak but measurable brittle extension; a substantial part of total deformation is probably aseismic or transferred to adjacent domains	Absolute amplitude is weakly resolved because bootstrap uncertainty is comparable to the mean
Northern Red Sea	~10^{-9} yr^{-1}	Geodetic and tectonic constraints require Arabia–Nubia divergence, but the earthquake-derived strain budget is very small	Very low seismic coupling; deformation is likely shared among small earthquakes, magmatic/dyking processes, and ductile or distributed deformation	The present PMTS analysis cannot uniquely separate dyking, creep, and lower-crustal flow
Gulf of Aqaba	~10^{-6} yr^{-1}	GPS/back-slip models resolve active left-lateral motion along the Gulf of Aqaba–Dead Sea Transform, with slip rates of the order of several mm yr^{-1} (Castro-Perdomo et al. 2022)	Largest seismic strain signal and strongest transform localization; some deformation remains aseismic, including possible creep, post-seismic relaxation, and lower-crustal relaxation	Velocity tensors are model-equivalent quantities and should not be interpreted as direct GPS slip rates

among episodic seismic faulting, distributed crustal adjustment, limited fault creep, and stress transfer from adjacent active zones, consistent with a mature rift system in deceleration rather than cessation. These interpretations are independently supported by regional stress-field inversion, which identifies normal-faulting regimes with NNE-SSW σ_3 in the Gulf of Suez and a strike-slip regime in the Gulf of Aqaba, both fully consistent with P-, T-, and B-axis geometries from our PMTS analysis. The convergence of two methodologically distinct approaches strengthens confidence in the inferred strain partitioning. Beyond corroborating stress orientations, the PMTS framework explicitly quantifies strain-rate magnitudes, propagates focal-mechanism uncertainties, and links seismic deformation directly to geodetic strain budgets. More broadly, the systematic seismic–geodetic discrepancy across all three domains underscores the dominant role of aseismic processes at this plate boundary, and the probabilistic approach offers a transferable tool for seismic strain partitioning and hazard assessment across other diffuse plate boundaries. The velocity tensors are retained as model-equivalent diagnostic outputs and should not be interpreted as direct substitutes for GPS velocities.

Acknowledgments This research was supported by the Ongoing Research Funding program (ORF-2026-425), King Saud University, Riyadh, Saudi Arabia. The software Generic Mapping Tools, developed by Wessel and Smith (1998), was used for data processing and mapping.

Author contributions A. A. conceived the study, developed the probabilistic moment tensor summation methodology, performed data processing, uncertainty analysis, visualization, and wrote the original manuscript draft. M. E. contributed to seismic data compilation, tectonic interpretation, and manuscript review. Ch. J. contributed to geological interpretation, regional tectonic framework development, and manuscript revision. H. A. supervised the research framework, contributed to scientific interpretation, and reviewed and edited the manuscript. All authors discussed the results and approved the final manuscript.

Funding This research was supported by the Ongoing Research Funding Program (ORF-2026–425), King Saud University, Riyadh, Saudi Arabia.

Data availability Earthquake catalogs and focal-mechanism datasets used in this study were compiled from previously published sources cited within the manuscript. Derived datasets generated during the current study, including probabilistic moment-tensor summation results and bootstrap uncertainty outputs, are available from the corresponding author upon reasonable request.

Declarations

Ethical approval This article does not contain any studies involving human participants or animals performed by any of the authors.

Consent to participate Not applicable.

Consent for publication All authors consent to the publication of this manuscript.

Competing interests The authors declare that they have no competing financial or non-financial interests related to this work.

References

Abd El-Aal AK, Mostafa S, Abdelhafiez HE (2019) Review of the seismotectonic setting of the Gulf of Aqaba with respect to the June 27 2015 and the May 16 2016 earthquake sequences. Pure Appl Geophys 176:541–562. https://doi.org/10.1007/s00024-018-2024-5

Abdalzaher MS, El-Hadidy M, Gaber H, Badawy A (2020) Seismic hazard maps of Egypt based on spatially smoothed seismicity model and recent seismotectonic models. J Afr Earth Sci 170:103894. https://doi.org/10.1016/j.jafrearsci.2020.103894

Abdelazim M, ElGabry MN, Gobashy MM, Khalil MH, Husseis HM (2023) Seismicity and fault interaction in the Gulf of Aqaba. Pure Appl Geophys 180:2045–2066. https://doi.org/10.1007/s00024-023-03279-x

Abu El-Nader IF, Hussein HM (2018) The present-day active deformation in the central and northern parts of the Gulf of Suez area, Egypt, from earthquake focal mechanism data. Nat Hazards 92:1355–1369. https://doi.org/10.1007/s11069-018-3254-7

Aki K, Richards PG (1980) Quantitative Seismology: Theory and Methods. W.H. Freeman, San Francisco

Al-Ahmadi K, Alamri A, See L (2014) A spatial statistical analysis of the occurrence of earthquakes along the Red Sea floor spreading: clusters of seismicity. Arab J Geosci 7:2893–2904. https://doi.org/10.1007/s12517-013-0974-6

Ali SM, Badreldin H (2019) Present-day stress field in Egypt based on a comprehensive and updated earthquake focal mechanisms catalog. Pure Appl Geophys 176:4729–4760. https://doi.org/10.1007/s00024-019-02262-9

Almalki KA, Betts PG, Ailleres L (2015) The Red Sea - 50 years of geological evolution. Earth-Sci Rev 147:109–140. https://doi.org/10.1016/j.earscirev.2015.05.002

Al-Shijbi Y, El-Hussain I, Deif A, Al-Kalbani A, Mohamed AM (2019) Probabilistic seismic hazard assessment for the Arabian Peninsula. Pure Appl Geophys 176:1503–1530. https://doi.org/10.1007/s00024-018-2033-4

ArRajehi A, McClusky S, Reilinger R et al (2010) Geodetic constraints on present-day motion of the Arabian Plate: implications for Red Sea and Gulf of Aden rifting. Tectonics 29:2009TC002482. https://doi.org/10.1029/2009TC002482

Artemieva IM, Yang H, Thybo H (2022) Incipient ocean spreading beneath the Arabian shield. Earth-Sci Rev 226:103955. https://doi.org/10.1016/j.earscirev.2022.103955

Augustin N, van der Zwan FM, Devey CW, Brandsdóttir B (2021) 13 million years of seafloor spreading throughout the Red Sea Basin. Nat Commun. https://doi.org/10.1038/s41467-021-22586-2

Badawy A (2005) Present-day seismicity, stress field and crustal deformation of Egypt. J Seismol 9(3):267–276. https://doi.org/10.1007/s10950-005-2190-7

Badawy A, Horváth F (1999) Seismicity of the Sinai subplate region. Tectonophysics 304:175–193. https://doi.org/10.1016/S0264-3707(98)00024-6

Badreldin H, Abdel-Aal AA, Toni M, El-Faragawy K (2019) Moment tensor inversion of small-to-moderate size local earthquakes in Egypt. J Afr Earth Sci 151:153–172. https://doi.org/10.1016/j.jafrearsci.2018.12.004

Ben-Avraham Z, Garfunkel Z, Lazar M (2008) Geology and evolution of the southern Dead Sea Fault with emphasis on subsurface structure. Annu Rev Earth Planet Sci 36:357–387. https://doi.org/10.1146/annurev.earth.36.031207.124201

Bosworth W, Huchon P, McClay K (2005) The Red Sea and Gulf of Aden basins. J Afr Earth Sci 43:334–378. https://doi.org/10.1016/j.jafrearsci.2005.07.020

Bosworth W, McClay K (2001) Structural and stratigraphic evolution of the Gulf of Suez rift, Egypt: a synthesis. In: Peri-Tethys Memoir 6: Peri-Tethyan Rift/Wrench Basins and Passive Margins. Mém Mus Natl Hist Nat 186:567–606

Bosworth W, Stockli DF (2016) Early magmatism in the northern Red Sea and its implications for the rifting process. Can J Earth Sci 53:653–669. https://doi.org/10.1139/cjes-2016-0019 [body cites as 'Bosworth et al., 2016' - change to 'Bosworth and Stockli, 2016']

Bosworth, W. (2015). Geological Evolution of the Red Sea: Historical Background, Review, and Synthesis. In: Rasul, N., Stewart, I. (eds) The Red Sea. Springer Earth System Sciences. Springer, Berlin, Heidelberg. https://doi.org/10.1007/978-3-662-45201-1_3

Camp VE, Roobol MJ (1992) Upwelling asthenosphere beneath western Arabia and its regional implications. J Geophys Res 97:15255–15271. https://doi.org/10.1029/92JB00943

Castro-Perdomo N, Viltres R, Masson F et al (2022) Interseismic deformation in the Gulf of Aqaba from GPS measurements. Geophys J Int 228:477–492. https://doi.org/10.1093/gji/ggab353

Chang SJ, Merino M, Van der Lee S et al (2011) Mantle flow beneath Arabia and the Red Sea. Earth Planet Sci Lett 302:144–152. https://doi.org/10.1016/j.epsl.2010.12.050

Cochran JR (2005) Northern Red Sea: nucleation of an oceanic spreading center within a continental rift. Geochem Geophys Geosyst 6:Q03006. https://doi.org/10.1029/2004GC000826

Coleman RG, McGuire AV (1988) Magma systems related to the Red Sea opening. Tectonophysics 150:77–100. https://doi.org/10.1016/0040-1951(88)90296-X

Corti G (2009) Continental rift evolution: from rift initiation to incipient break-up in the Main Ethiopian Rift, East Africa. Earth Sci Rev 96(1–2):1–53. https://doi.org/10.1016/j.earscirev.2009.06.005

Deif A, Al-Shijbi Y, El-Hussain I, Ezzelarab M, Mohamed AME (2017) Compiling an earthquake catalogue for the Arabian Plate, Western Asia. J Asian Earth Sci 147:345–357. https://doi.org/10.1016/j.jseaes.2017.07.033

Ebinger CJ, Sleep NH (1998) Cenozoic magmatism throughout east Africa resulting from impact of a single plume. Nature 395:788–791. https://doi.org/10.1038/27417

El Khrepy S, Koulakov I, Gerya T, Al-Arifi N, Alajmi MS, Qadrouh AN (2021) Transition from continental rifting to oceanic spreading in the northern Red Sea area. Sci Rep 11:5594. https://doi.org/10.1038/s41598-021-84952-w

El-Hussain I, Al-Shijbi Y, Deif A, Mohamed AME, Ezzelarab M (2018) Developing a seismic source model for the Arabian Plate. Arab J Geosci 11:435. https://doi.org/10.1007/s12517-018-3797-7

Ezzelarab M, Shokry MMF, Mohamed AME, Helal AMA, Mohamed AA, El-Hadidy MS (2016) Evaluation of seismic hazard at the northwestern part of Egypt. J Afr Earth Sci 113:114–125. https://doi.org/10.1016/j.jafrearsci.2015.10.017

Fernández-Blanco D, de Gelder G, Jackson CAL (2025) Is the Suez Rift in its post-rift phase? Geophys Res Lett. https://doi.org/10.1029/2025GL117313

Furlong KP, Schwartz SY (2004) Influence of the Mendocino triple junction on the tectonics of coastal California. Annu Rev Earth Planet Sci 32:403–433. https://doi.org/10.1146/annurev.earth.32.101802.120252

Hamimi Z, El-Barkooky A, Martínez Frías J, Fritz H, Abd El-Rahman Y (eds) (2020) The Geology of Egypt. Regional Geology Reviews, Springer.https://doi.org/10.1007/978-3-030-15265-9

Hanks TC, Kanamori H (1979) A moment magnitude scale. J Geophys Res Solid Earth 84(B5):2348–2350. https://doi.org/10.1029/JB084iB05p02348

Hofstetter R, Beyth M (2003) The Afar Depression: interpretation of the 1960–2000 earthquakes. Geophys J Int 155:715–732. https://doi.org/10.1046/j.1365-246X.2003.02080.x

Hofstetter A, Klinger Y, Amrat AQ, Rivera L, Dorbath L (2007) Stress tensor and focal mechanisms along the Dead Sea fault and related structural elements based on seismological data. Tectonophysics 429:165–181. https://doi.org/10.1016/j.tecto.2006.03.010

Hussein HM, Abou Elenean KM, Marzouk IA, Korrat IM, Abu El-Nader IF, Ghazala HH, ElGabry MN (2013) Present-day tectonic stress regime in Egypt and surrounding area based on inversion of earthquake focal mechanisms. J Afr Earth Sci 81:1–15. https://doi.org/10.1016/j.jafrearsci.2012.12.002

Ibrahim E, Abd El-Motaal E, Lashin A, Alfaifi H, Qaysi S, Kahal A (2021) Faulting intersections and magma-feeding zones in Tihamat-Asir, Southeast Red Sea rift: aeromagnetic and structural perspective. J Afr Earth Sci 173:104044. https://doi.org/10.1016/j.jafrearsci.2020.104044

Izzeldin AY (1987) Seismic, gravity and magnetic surveys in the central part of the Red Sea: their interpretation and implications for the structure and evolution. Tectonophysics 143:269–306. https://doi.org/10.1016/0040-1951(87)90214-9

Jackson J, McKenzie D (1988) The relationship between plate motions and seismic moment tensors, and the rates of active deformation in the Mediterranean and Middle East. Geophys J 93:45–73. https://doi.org/10.1111/j.1365-246X.1988.tb01387.x

Kaviani A, Paul A, Moradi A et al (2020) Mantle structure beneath the Arabian Peninsula from Rayleigh wave tomography. Geophys J Int 222:1777–1795. https://doi.org/10.1093/gji/ggaa075

Kiratzi A, Benetatos C, Vallianatos F (2018) Seismic Deformation Derived from Moment Tensor Summation: Application Along the Hellenic Trench. In: D'Amico, S. (eds) Moment Tensor Solutions. Springer Natural Hazards. Springer, Cham. https://doi.org/10.1007/978-3-319-77359-9_10

Koptev A, Burov E, Gerya T, Le Pourhiet L, Leroy S, Calais E, Jolivet L (2018) Plume-induced continental rifting and break-up in ultra-slow extension context: insights from 3D numerical modeling. Tectonophysics 746:121–137. https://doi.org/10.1016/j.tecto.2017.03.025

Le Béon M, Klinger Y, Amrat AQ et al (2008) Slip rate and locking depth along the Dead Sea Fault in the Gulf of Aqaba. J Geophys Res 113:B11403. https://doi.org/10.1029/2007JB005280

Luis JF, Miranda JM (2008) Reevaluation of magnetic chrons in the North Atlantic between 35 degrees N and 47 degrees N: implications for the formation of the Azores Triple Junction and associated plateau. J Geophys Res 113:B10105. https://doi.org/10.1029/2007JB005573

Masson F, Hamiel Y, Agnon A, Klinger Y, Deprez A (2015) Variable behavior of the Dead Sea Fault along the southern Arava segment from GPS measurements. C R Geosci 347(4):161–169. https://doi.org/10.1016/j.crte.2014.11.001

McClusky S, Reilinger R, Mahmoud S et al (2003) GPS constraints on the kinematics of the Arabia-Eurasia collision zone. Geophys J Int 155:419–434. https://doi.org/10.1046/j.1365-246X.2003.02023.x

McGuire AV, Bohannon RG (1989) Timing of the Red Sea rifting and the development of the Arabian Sea. J Geophys Res 94:1677–1691. https://doi.org/10.1029/JB094iB02p01677

McQuarrie N, Stock JM, Verdel C, Wernicke BP (2003) Cenozoic evolution of the Zagros and the Red Sea. Tectonics 22:1069. https://doi.org/10.1029/2003TC001530

Moawad MB et al (2025) Superposed deformation in the southern Gulf of Suez rift and impact on hydrocarbon maturation. Mar Pet Geol 178:107639. https://doi.org/10.1016/j.marpetgeo.2025.107639

Molnar P (1979) Earthquake recurrence intervals and seismic moment. Bull Seismol Soc Am 69:115–133. https://doi.org/10.1785/BSSA0690010115

Morley CK (ed) (1999) Geoscience of Rift Systems - Evolution of East Africa. AAPG Studies in Geology 44. https://doi.org/10.1306/St44623

Morsy M, Hussein HM, Abou Elenean KM, El-Hady S (2011) Stress field in the central and northern parts of the Gulf of Suez area, Egypt from earthquake fault plane solutions. J Afr Earth Sci 60:293–302. https://doi.org/10.1016/j.jafrearsci.2011.03.006

Park Y, Nyblade AA, Rodgers AJ, Al-Amri A (2007) Upper mantle structure beneath the Arabian Peninsula and northern Red Sea

from teleseismic body wave tomography. Geochem Geophys Geosyst 8:Q06021. https://doi.org/10.1029/2006GC001566

Petrunin AG, Kaban MK, El Khrepy S, Al-Arifi N (2020) Mantle convection patterns reveal the mechanism of the Red Sea rifting. Tectonics 39:e2019TC005829. https://doi.org/10.1029/2019TC005829

Reilinger R, McClusky S (2011) Nubia-Arabia-Eurasia plate motions and the dynamics of the Mediterranean and Middle East. Geophys J Int 186:799–815. https://doi.org/10.1111/j.1365-246X.2011.05133.x

Reilinger R, McClusky S, Vernant P et al (2006) GPS constraints on continental deformation in the Africa-Arabia-Eurasia collision zone and implications for plate dynamics. J Geophys Res 111:B05411. https://doi.org/10.1029/2005JB004051

Richardson M, Arthur MA (1988) The Gulf of Suez-northern Red Sea Neogene rift: a quantitative basin analysis. Mar Pet Geol 5:247–270. https://doi.org/10.1016/0264-8172(88)90005-0

Said R (2017) The Geology of Egypt. Routledge, London (reprint). https://doi.org/10.1201/9780203736678

Salamon A, Hofstetter A, Garfunkel Z, Ron H (2003) Seismotectonics of the Sinai subplate - the eastern Mediterranean region. Geophys J Int 155:149–173. https://doi.org/10.1046/j.1365-246X.2003.02017.x

Sawires R, Peláez JA (2025) A reassessment of the seismic hazard for the Eastern Mediterranean region including the Gulf of Aqaba–Dead Sea Transform fault. In: Hamimi Z (ed) Seismotectonics of the East Mediterranean–Red Sea Region (Advances in Science, Technology & Innovation). Springer, Cham. https://doi.org/10.1007/978-3-031-80928-6_22

Sawires R, Peláez JA, Ibrahim HA, Fat-Helbary RE (2016a) Delineation and characterization of a new seismic source model for seismic hazard studies in Egypt. Nat Hazards 80:1823–1864. https://doi.org/10.1007/s11069-015-2034-x

Sawires R, Peláez JA, Fat-Helbary RE, Ibrahim HA (2016b) Updated probabilistic seismic hazard values for Egypt. Bull Seismol Soc Am 106:1788–1801. https://doi.org/10.1785/0120150218

Schettino A, Macchiavelli C, Pierantoni PP, Zanoni D (2016) Recent kinematics of the Red Sea and Gulf of Aden. Geophys J Int 207:1870–1892. https://doi.org/10.1093/gji/ggw280

Thybo H, Nielsen CA (2009) Magma-compensated crustal thinning in continental rifts. Nature 457:873–876. https://doi.org/10.1038/nature07688

Voggenreiter W, Hötzl H, Mechie J (1988) Low-angle normal faults in the Red Sea Hills, Sudan. Tectonophysics 150:173–197. https://doi.org/10.1016/0040-1951(88)90011-X

Wright TJ, Ebinger C, Biggs J, Ayele A, Yirgu G, Keir D, Stork A (2006) Magma-maintained rift segmentation at continental rupture in the 2005 Afar dyking episode. Nature 442(7100):291–294. https://doi.org/10.1038/nature04978

Yao Q, Liu L, Wang K (2017) Mantle dynamics and the Red Sea rifting. J Geophys Res Solid Earth 122:7480–7498. https://doi.org/10.1002/2016JB013805

Publisher's Note Springer Nature remains neutral with regard to jurisdictional claims in published maps and institutional affiliations.

Springer Nature or its licensor (e.g. a society or other partner) holds exclusive rights to this article under a publishing agreement with the author(s) or other rightsholder(s); author self-archiving of the accepted manuscript version of this article is solely governed by the terms of such publishing agreement and applicable law.